Alma Mater Studiorum – Università di Bologna

School of Science

Department of Industrial Chemistry "Toso Montanari"

Corso di Laurea Magistrale / Master

Advanced Spectroscopy in Chemistry

Classe LM-71 - Scienze e Tecnologia della Chimica Industriale

Ex situ X-Ray Absorption Study of Li-rich Layered Cathode Material $Li[Li_{0.2}Mn_{0.56}Ni_{0.16}Co_{0.08}]O_2$

Candidate: Diandian Wang

Tutor: Prof. Dr. Marco Giorgetti

First Session
Academic Year 2012-2013

Alma Mater Studiorum – Università di Bologna

Ex situ X-Ray Absorption Study of Li-rich Layered Cathode Material $Li[Li_{0.2}Mn_{0.56}Ni_{0.16}Co_{0.08}]O_2$

Candidate:

Diandian Wang

Tutor:

Prof. Dr. Marco Giorgetti

First Session

Academic Year 2012-2013

TABLE OF CONTENTS

LIST OF FIGURES

LIST OF TABLES

ABSTRACT

The Li-rich layered transition metal oxides (LLOs) Li_2MnO_3-$LiMO_2$ (M=Mn, Co, Ni, *etc*.) have drawn considerable attention as cathode materials for rechargeable lithium batteries. They generate large reversible capacities but the fundamental reaction mechanism and structural perturbations during cycling remain controversial. In the present thesis, *ex situ* X-ray absorption spectroscopy (XAS) measurements were performed on $Li[Li_{0.2}Mn_{0.56}Ni_{0.16}Co_{0.08}]O_2$ at different stage of charge during electrochemical oxidation/reduction. K-edge spectra of Co, Mn and Ni were recorded through a voltage range of 3.7-4.8V *vs*. Li/Li^+, which consist of X-ray absorption near edge structure (XANES) and extended X-ray absorption fine structure (EXAFS). Oxidation states during initial charge were discussed based on values from literature as well as XANES analysis. Information about bond distance, coordination number as well as corresponding Debye-Waller factor were extracted from Gnxas analysis of raw data in the EXAFS region. The possibility of oxygen participation in the initial charge was discussed. Co and Ni prove to take part in the oxidation/reduction process while Mn remain in the tetravalent state. The cathode material appears to retain good structural short-range order during charge-discharge. A resemblance of the pristine sample and sample 4 was discovered which was firstly reported for similar compounds.

1. Introduction

The demand for advanced energy storage devices has increased significantly each year for the past decade. They are motivated by a variety of different needs but all have in common the potential benefits for our technologically driven, highly mobile, energy challenged society. Addressing the more pressing needs will be driven by the efficient use of renewable energies where energy storage provides critical load leveling. The requirements of the appropriate energy storage device differ notably for each application; hence research in the field of rechargeable batteries has intensified in the past decade in attempt to meet these demands. [1]

Among the various existing technologies, Li-based batteries, because of their high energy density and design flexibility, currently outperform other systems, accounting for 63% of worldwide sales by values in portable batteries. [2] Recent developments in negative electrode materials require higher capacity positive electrodes to provide optimum utilization of the storage properties. $LiCoO_2$ has been most widely used in commercial Li-ion batteries because of its good electrochemical performance. However, it suffers from several drawbacks such as high cost, toxicity and safety problems. The cutoff voltage is limited to around to 4.2V in avoidance of rapid capacity loss, [3] which inhibit its further use in hybrid and pure electric vehicles. Several routes were investigated to circumvent these safety and capacity issues. Among them was the successful stabilization of a solid solution of layered Li_2MnO_3 and $LiMO_2$ (M=Mn, Co, Ni, *etc*.), which exhibit relatively high capacity, low cost and improved safety.

In the present work we report the structural analysis of layered Li-rich NCM: $Li[Li_{0.2}Mn_{0.56}Ni_{0.16}Co_{0.08}]O_2$, which can also be seen as the solid solution of Li_2MnO_3 and $LiMn_{0.4}Ni_{0.4}Co_{0.2}O_2$ in 6:4 molar ratio, using X-ray absorption spectroscopy (XAS). XAS is a powerful tool that provides information on a very local scale (4-5Å). More importantly, since the interaction of X-rays with any given atomic species (i.e., absorption) is an energy-dependent phenomenon, XAS allows us to probe the local environment of the selected element of interest only.

2. Battery

2.1 Lithium-Ion Battery (LIB)

Lithium-ion batteries have been considered a near-term solution for energy shortage on account of their high energy density and relatively simple reaction mechanism. It first emerged in the early 1900s as lithium batteries in the pioneer work by G.N. Lewis *et al*. Due to the inherent instability of lithium metal, attempts to develop rechargeable lithium battery failed but shifted to a non-metallic lithium battery using lithium ions. [4] Although slightly lower in energy density, it enjoys much better safety conditions, which lays the foundation for mass commercial production. For over twenty years, Li-ion rechargeable battery has been well developed and widely used in the portable equipment market like cameras, cell phones and laptops, almost totally replacing the conventional alkaline, lead acid and Ni-Cd batteries. Nevertheless, to be employed in the large-scale high-power system such as the plug-in hybrid electric vehicle (PHEV) or plug-in electric vehicle (PEV), lithium-ion batteries with better performance than existing ones are urgently called for, especially in regards to energy density, cycling life and safety issues.

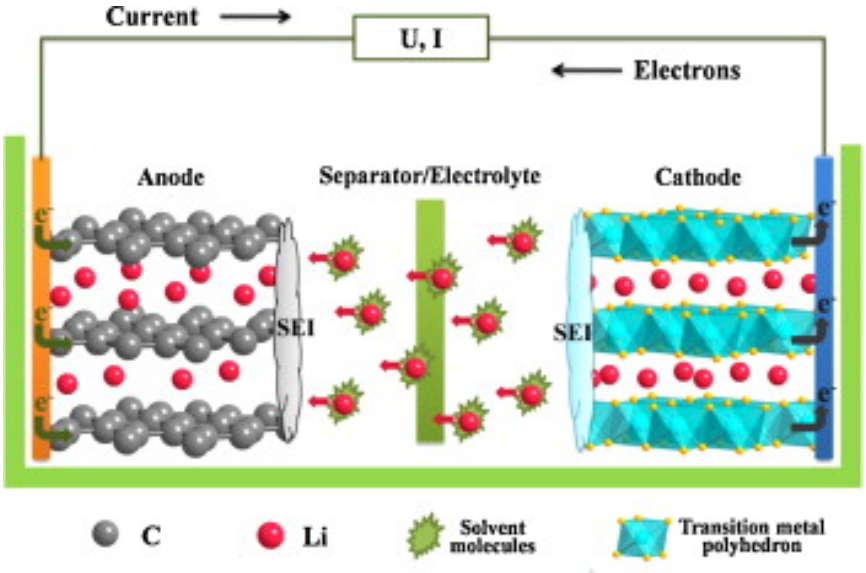

Fig. 1 Working mechanism of LIB system during charging.

Battery is composed of several electrochemical cells that are connected in series or in parallels to provide the required voltage and capacity. [1] They serve as energy storage device by converting electric energy into electrochemical energy. The fundamental working mechanism of one typical battery cell can be found in Fig. 1. It

consists of three major components: a positive cathode (cathode), a negative electrode (anode) separated by an electrolyte, which enables ion transfer between the two electrodes. For today's commercialized LIB system, both cathode and anode materials are insertion materials. The most common active material for anode is graphite while for cathode, transition metal oxides and metal phosphates are mostly employed. Both of them possess largely unchangeable hosts with specific sites for Li ions to be intercalated and deintercalated during cycling.

During the charging process, Li ions are extracted from the cathode host, move through the non-aqueous electrolyte, and intercalate into the anode sheet in the anode. In the mean time, electrons are also liberated and move from cathode to anode through the outside current collectors enabling the current to be tapped by the user. During this process, electric energy is transformed into electrochemical energy since the chemical potential of Li is much higher in the anode than in the cathode. The electrochemical energy is again released in the form of electric energy during discharge.

The cathode and anode electrolytes are separated by a micro-porous membrane that allows the electrolyte to penetrate and prevents shorting between the two electrodes. [5] The electrolyte should be ionically conducting and electronically insulating at the same time. However, the actual chemical reactions the electrolyte undergoes is much more complicated. During the first charge, a passivation film, called solid–electrolyte-interphase (SEI) layer builds up on the graphite/electrolyte interface at extreme voltage range (typically <1.2 V or >4.6 V). It is proposed due to reaction of Li^+ ions with degradation products of the electrolyte that ultimately leads to the deposition of insoluble solid parts on the anode surface. A densely packed ideal SEI effectively prevents the graphite structure from decomposition and allows cycling of lithium batteries without major capacity fades. [6]

In current LIB technology, the energy density, which comprises cell voltage and reversible capacity, is mainly determined by the cathode material. It is also a crucial factor for Li transportation rate. Besides, cathode material is usually the most expensive material with the highest weight inside a battery, all of which justify the intense research focus on the cathode in recent decades.

Since the investigated on $LiCoO_2$ as a candidate cathode material for rechargeable lithium ion battery in 1980, transition metal oxides have attracted extensive research interest. They are basically categorized into six structural groups, including: layered compounds $LiMO_2$ (M=Co, Ni, Mn, *etc*.), spinel compounds LiM_2O_4 (M=Mn, *etc*.), olivine compounds $LiMPO_4$ (M=Fe, Mn, Ni, Co, *etc*.), silicates, borates and

tavorites [5] with each group having distinct characteristics. There exists several criterions during material optimization and development: (1) energy density, which is determined by reversible capacity and operating voltage, relies mostly on the intrinsic chemistry like effective redox couples and maximum lithium concentration in the active material; (2) cell dynamics, namely rate capability and cycling performance, where electronic and ionic mobilities are the key determining factors; (3) safety and cost. Consequently, material optimization is usually made from two approaches: modify the morphology and change the intrinsic chemistry.

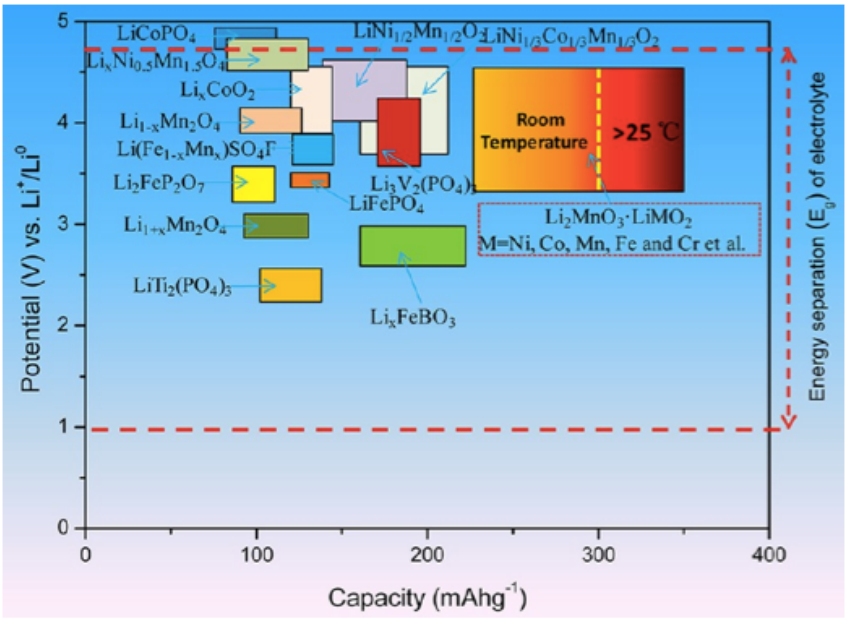

Fig. 2 Voltage and capacity of the main cathode materials for lithium-ion batteries under investigation. [7]

In the present work, the lithium-rich layered oxide is the material of choice because of its high capacity (Fig. 2). They are able to deliver a capacity of more than 280 mAh/g with higher operating voltage (> 3.5V *vs.* Li/Li^+). Detailed introduction of the layered compound $LiMO_2$ will be presented in Chapter 2.2.

2.2 Layered Compound $LiMO_2$

2.2.1 Development

Before the lithium-rich layered oxide materials (LLOs) were extensively investigated, the layered li-ion batteries went through several major stages of development. $LiCoO_2$ was introduced as possible candidate for rechargeable lithium

batteries, deintercalating and intercalating Li around 4V. [1] However it can only deliver a reversible capacity of about 140mAh/g which is half of its theoretical value (~270mAh/g). [3] It is proposed to due to structural instability of the cathode during delithiation. The presence of toxic Co also bring about safety issues as well as environmental problems. Research focus thus moved to more abundant and environmental friendly transition metals in replacement of Co, such as Mn and Ni.

The methods included mixing $LiMnO_2$ and $LiNiO_2$ in a 1:1 ratio, forming layered $LiMn_{0.5}Ni_{0.5}O_2$. It was firstly reported by Ohzuku *et al*. in 2001. [8] They generally exhibit an improved capacity (~200mAh/g) at charge-discharge voltage around 3.6-4.3V with little capacity fading even after 100 circles. X-ray Absorption Spectroscopy (XAS) confirmed Ni^{2+}/Ni^{4+} as active redox couple. Structural characterization of samples during cycling showed a migration of around 8-10% Ni ions to the Li layer, which was also confirmed by first-principles calculation. [7] The Li-Ni interlayer mixing attributes to the relatively large capacity by enhancing structural stability during Li extraction and insertion. On the other hand, large amount of Ni in the Li layer block Li diffusion pathways, resulting in a low rate capability. [9]

Attempts were made to improve Li mobility of the material for better rate capability. $LiCo_{1/3}Mn_{1/3}Ni_{1/3}O_2$ was found to be a good substitution. Extra amount of Co serves to reduce Ni content in the Li layer to 1-6%. Same reversible capability was achieved with an extended voltage window to 3.6-3.7V. [10] It was believed that both Ni and Co ion acted as redox couple with Ni being oxidized from Ni^{2+} to Ni^{4+} and Co being oxidized from Co^{3+} to Co^{4+} while the oxidation state of Mn remained unchanged. Electrons were also proposed to be removed from oxygen 2p orbital due to the orbital overlap with metal 3d band, leading up to oxygen release at high charging voltage.

It was also discovered that the introduction of extra amount of Li ion could greatly improve material capacity (~250mAh/h). A serious of lithium-rich layered oxide materials were created consisted of a layered $Li[Li_{1/3}Mn_{2/3}]O_2$ (generally denoted as Li_2MnO_3) and $LiMO_2$ (M: 3d-transition metals, such as Mn, Ni, CO, Fe, Cr, *etc*.). Their structural compatibility as rock-salt structures allows for the structural integration. They can also be formulated as zLi_2MnO_3-$(1-z)LiMO_2$ proposed by Thackeray *et al*., or even $Li[Li_{x/3}M_{1-x}Mn_{2x/3}]O_2$ ($0<x<1$), where the elements in the brackets represent the composition of the transition metal slab. Its capabilities of delivering a high capacity of over 250mAh/g are believed owe to the presence of monoclinic Li_2MnO_3 domain within a $LiMO_2$ matrix, which serves to stabilize the structure of the $LiMO_2$ phase during Li extraction. [11] But other researchers argue

that the two components Li_2MnO_3 and $LiMO_2$ coexist as a solid solution. The compound $Li[Li_{1/9}Ni_{1/3}Mn_{5/9}]O_2$ was firstly reported by Lu *et al*. in 2001. [12] Compounds with different Li/M content were also studied and similar electrochemical performance were revealed. When Li_2MnO_3 was found to be electrochemically activated by charging over 4.5V, $xLi_2MnO3\text{-}(1\text{-}x)LiMO_2$ became more and more appealing. A distinct plateau was observed on the voltage profile when charged around 4.5-4.6V, which does not appear in the following charge/discharge cycles. The mechanism of the abnormally high voltage capacity still remains controversial, [13] the details of which will be discussed in section 2.2.3 of "Reaction Mechanism". In spite of the favored capacity, lithium-rich layered oxide materials suffer from poor rate capability caused by significant number of transition metal ions in the lithium layer. [14]

2.2.2 Local Structure

In this part, two popular hypotheses of local structures, *e.g*., coexistence of two phases and homogeneous solid solutions are discussed.

An ideal structure of layered $LiMO_2$ can be seen in Fig. 3 with Li layer and MO_2 slabs stacked alternatively. Oxygen anions form a close-packed fcc lattice with metal cations located in the 6-coordinated octahedral crystal sites.

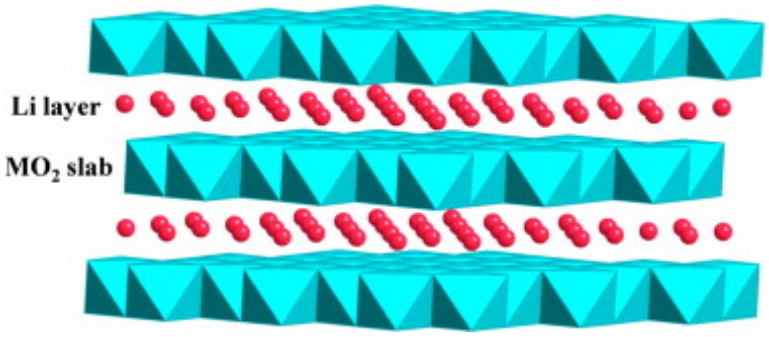

Fig. 3 Crystal structure of layered $LiMO_2$. Oxygen ions are omitted for clarity. [5]

More comprehensive crystal structures of $LiMO_2$ and Li_2MnO_3 are shown in :

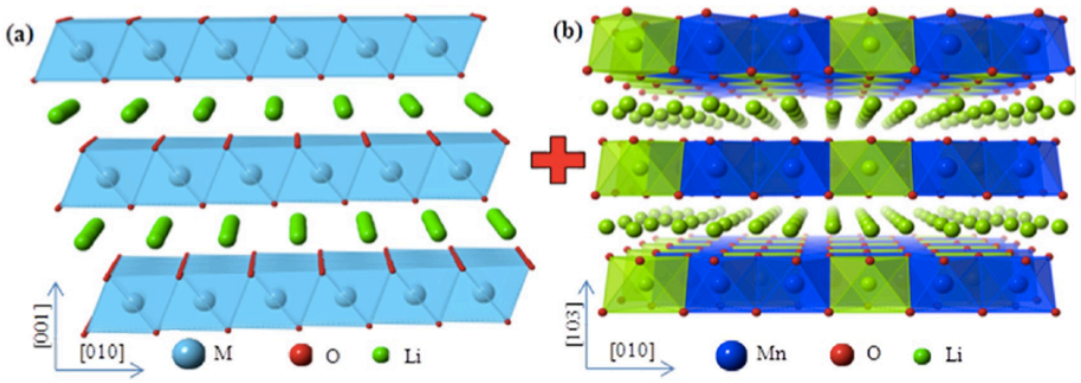

Fig. 4 Crystal structure of (a) rhombohedral (space group: $R\bar{3}m$) $LiMO_2$ and (b) monoclinic (space group: C2/m) Li_2MnO_3 viewed from [100] crystallographic direction. [7]

It is evident that the monoclinic Li_2MnO_3 structure resembles that of $LiMO_2$ in terms of a layered configuration of Li and metal alternatively. Li_2MnO_3 can actually be considered a particular case of $LiMO_2$ with M layer composed of a periodic arrangement of one Li for every two Mn atoms (Li-Mn-Mn). A multitude of experimental characterizations have been done in support of this argument. One study by synchrotron X-ray diffraction (SXRD) [15] showed a good Rietveld structure refinement if a two-phases model was selected. Phase fraction of the rhombohedral and monoclinic components proved to be 43% and 57% respectively. Results of high-resolution transmission electron microscopy spectroscopy (HRTEM), [16] high-angle annular dark field scanning transmission electron microscopy (HAADF-STEM) [17] and Li magic-angle spinning (MAS) nuclear magnetic resonance (NMR) [18,19] also confirmed the Li_2MnO_3-like region in the parent rhombohedral framework, even though probably quasi-randomly distributed.

Much as the various evidence of two-phase arrangement of LLOs, some researchers believe a homogeneous solid solution model for $xLi_2MnO3{\cdot}(1\text{-}x)LiMO_2$ since lattice parameters appear to change linearly with composition of the $LiMO_2$ component. [19] Proposed structure can be seen in Fig. 5.

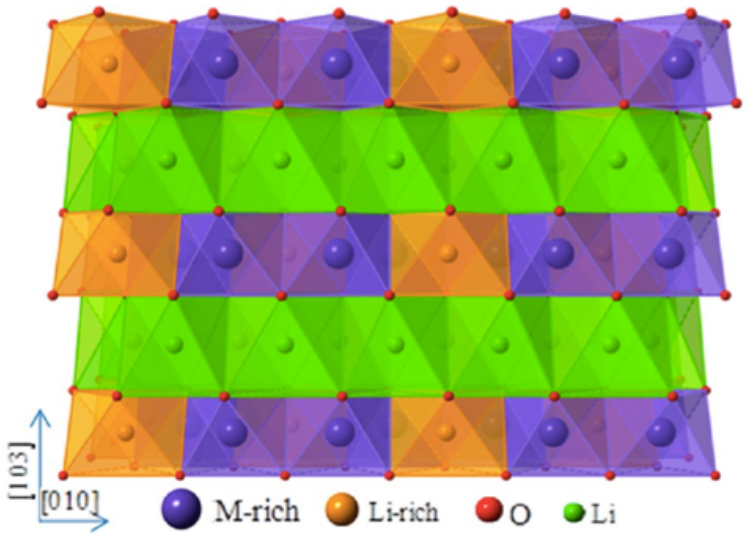

Fig. 5 Crystal structure of homogeneous solid solution with partial ordered C2/m monoclinic phase viewed from the [100] crystallographic direction.

Holding the same opinion of a solid solution conformation, scientists differ in their viewpoints of the crystal symmetries of those LLOs. Both rhombohedral and monoclinic symmetry for the solid solution were proposed and investigated. [20] Jarvis *et al*. carefully investigated into $Li[Li_{0.2}Ni_{0.2}Mn_{0.6}]O_2$ and concluded a partial solid solution. [21] They showed a monoclinic (C2/m) structure with Li-ordering. But they noted that materials with less excess lithium may results in two-phase regions due to lack of ordering between Li^+ and Mn^{4+} in the transition-metal layer. As a matter of fact, raw material, preparation methods, as well as calcination temperatures could all be an influential factor. More extensive investigations are still in great need to reveal atomic structure of Li-rich layered oxide materials of different compositions.

2.2.3 Reaction Mechanism

For lithium-rich layered oxide materials, it is generally accepted that the charging process is associated with oxidation of transition metals to a tetravalent state as well as lithium extraction. Consequently, Li_2MnO_3, where Mn exist in their tetravalent state, is considered electrochemically inactive as electrode material during the first charge. Major metal oxidation takes place at voltage plateaus on the voltage profile. A well-defined plateau could be observed at 4.5-4.6V upon initial charge accompanied by a large amount of Li extraction. However, such plateau does not exist in the following circles, causing a large irreversible capacity. The corresponding reaction mechanism has been extensively investigated but still under

debate. Li^+ and O^{2-} removal has been reported by Lu *et al*. based on Rietveld analysis, generating oxygen vacancies in the crystal lattice. [22] Other researches proposed surface reaction with electrode/electrolyte reduction and Li^+/H^+ exchange at elevated temperature. [23]

A change in crystal structure is believed to accompany the oxygen removal process. Armstrong *et al*. [24] put forward a cation migration model where transition metals migrate from the surface into the bulk and occupy the vacancies created by Li removal when oxygen is simultaneously removed from the material surface. Neutron diffraction combined with the in situ differential electrochemical mass spectrometry (DEMS) was utilized for material characterization. A similar "lattice densification" model was also proposed on the basis of the analytical results obtained by XRD. [25] Recent researches also suggested electrochemically active Li ion in the transition metal layer that migrate to Li layer during charging and become stable tetrahedral ions. [26,27] The "caution migration process" has been further confirmed by Xu *et al*. using first principle calculations. [5]

3. X-ray Absorption Spectroscopy

3.1 Background

X-ray absorption fine structure (XAFS) spectroscopy is a powerful tool that provides information on a very local scale (4-5Å) and is well suited for the characterization of not only crystals, but also materials that possess little or no long-range translational order. More importantly, since the interaction of X-ray with any given atomic species (*i.e.*, absorption) is an energy-dependent phenomenon, XAFS allows us to probe the local structure around only selected elements that are contained within a material. The element-specific characteristic of XAFS, providing both chemical and structural information at the same time, differentiates it from the other techniques. In this respect, it serves as a unique tool for the investigation of battery materials during charge-discharge circles.

X-rays are light waves with energies ranging from about 500 eV to 100keV. In this energy regime, light is absorbed by all matter through the photoelectric effect mainly. In this process, an X-ray photon is absorbed by an electron in a tightly bound quantum core level of an atom (Fig. 6)

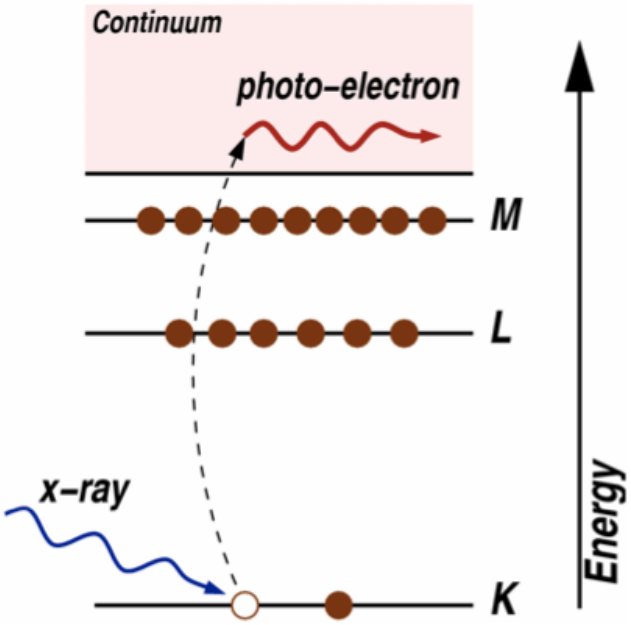

Fig. 6 Scheme of photoelectric effect.

When discussing X-ray absorption, we are primarily concerned with the absorption coefficient μ, which gives the probability that X-rays will be absorbed according to Beer's Law:

$$I = I_0 e^{-\mu t} \tag{1}$$

where I_0 is the intensity of X-ray incident on a sample, t is the sample thickness, and I is the intensity transmitted through the sample, as shown in Fig. 7. For X-rays, as for all light, the X-ray intensity is proportional to the number of X-ray photons.

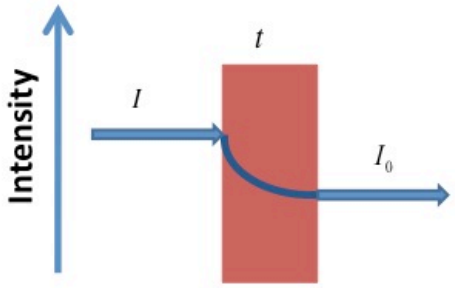

Fig. 7 Scheme of X-ray absorption measurement.

At most X-ray energies, the absorption coefficient μ is a smooth function of energy, with a value that depends on the sample density ρ, atomic number Z, atomic mass A and the X-ray energy E, roughly expressed as

$$\mu \approx \frac{\rho Z^4}{AE^3} \tag{2}$$

Due to its Z^4 dependence, the absorption coefficients of different elements exhibit big discrepancies, (spanning several orders of magnitude) so a good contrast between different materials can be achieved for any sample thickness and concentrations by adjusting the X-ray energy.

In order for a particular electronic core level to participate in the absorption, the binding energy of this core level must be less than the energy of the incident X-ray. If the binding energy is greater than the energy of the X-ray, the bound electron will not be perturbed from the well-defined quantum state and will not absorb the X-ray. If the binding energy of the electron is less than that of the X-ray, the electron may

be removed from its quantum level. In this case, the X-ray is absorbed and any energy in excess of the electronic binding energy is given to a photoelectron that is ejected from the atom. The implication of this process, *i.e.* photoelectric effect, lays the theoretical foundation for XAFS.

When the incident x-ray has an energy equal to that of the binding energy of a core level electron, there is a sharp rise in absorption: an absorption edge corresponding to the promotion of this core level to the continuum. An XAFS measurement is simply a measure of the energy dependence of μ at and above the binding energy of a known core level of a known atomic species. Since every atom has core level electrons with well-defined binding energies, we can select the element to probe by tuning the X-ray energy to an appropriate absorption edge. These absorption edge energies are already known (usually to within a tenth of percent) and tabulated. The edge energies vary with atomic number approximately as a function of Z^2, and both K and L levels can be used in the hard x-ray regime (in addition, M edges can be used for heavy elements in the soft x-ray regime), which allows most elements to be probed by XAFS with x-ray energies between 5 and 35 keV. Because the element of interest is chosen in the experiment, XAFS is element-specific.

Following an absorption event, the atom is said to be in an excited state, with one of the core electron levels left empty (a so-called core hole) and a photoelectron. The excited state will eventually decay typically within a few femtoseconds of the absorption event. Though this decay does not affect the x-ray absorption process, it is important for the discussion below.

There are two main mechanisms for the decay of the excited atomic state following an x-ray absorption event. The first of these is x-ray fluorescence (Fig. 8 left), in which a higher energy electron core-level electron fills the deeper core hole, ejecting an x-ray of well-defined energy. The fluorescence energy emitted in this way is characteristic of the atom, and can be used to identify the atoms in a system, and to quantify their concentrations. For example, an L shell electrons dropping into the K level give the Kα fluorescence line.

The second process for de-excitation of the core hole is the Auger Effect (Fig. 8 right), in which an electron drops from a higher electron level and a second electron is emitted into the continuum (and possibly even out of the sample). In the hard x-ray regime (> 2 keV), x-ray fluorescence is more likely to occur than Auger emission, but for lower energy x-ray absorption, Auger process dominates. Either of these processes can be used to measure the absorption coefficient μ, although the use of fluorescence is somewhat more common.

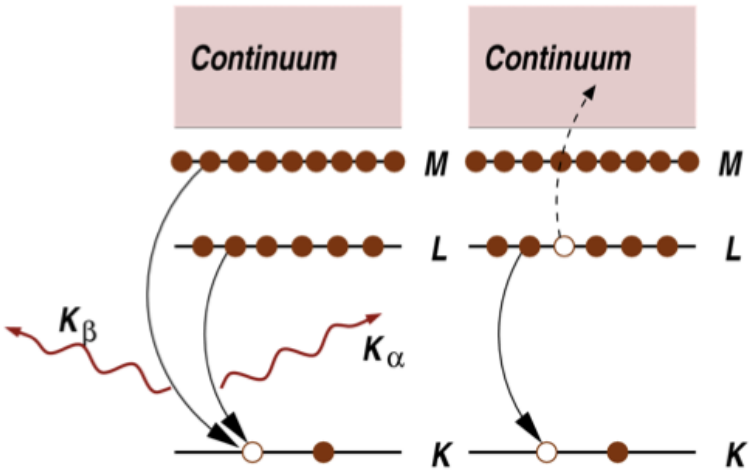

Fig. 8 Decay of the excited state: X-ray fluorescence (left) and Auger effect (right).

XAFS can be measured either in transmission or fluorescence geometries (The geometry for Auger measurements is typically the same as for fluorescence). Energy dependence of the absorption coefficient μ(E) in transmission and fluorescence are shown in Equation (3) and (4).

$$\mu(E) = log(I_0/I) \tag{3}$$

$$\mu(E) \propto I_f/I_0 \tag{4}$$

where I_f is the monitored intensity of a fluorescence line associated with the absorption process.

A typical XAFS spectrum (measured in the transmission geometry on Co edge) is shown in Fig. 9. The sharp discontinuous rise in μ(E) at 7709 eV due to the Co 1s electron level is clearly visible in the spectra, as are the oscillations in μ(E) above the edge. XAFS is generally thought of in two distinct portions: the X-ray near edge structure (XANES) – typically within 30eV of the main absorption edge, and the extended X-ray absorption fine structure (EXAFS). The distinction between XANES and EXAFS remains arbitrary, since the basic physical description of these two regimes is the same and there is no unambiguous definition that distinguishes between the "near edge" and "extended" structure. But some important approximations and limits allow us to interpret the extended spectra in a more quantitative way than is currently possible for the near edge spectra. EXAFS are normally used for quantitative determination of bond length and coordination

number thanks to its sensitivity to radial distribution of electron density around the absorbing atom, while XANES region provides information about oxidation state and geometry. Further introduction of both regions are presented in chapter 3.3 and 3.4.

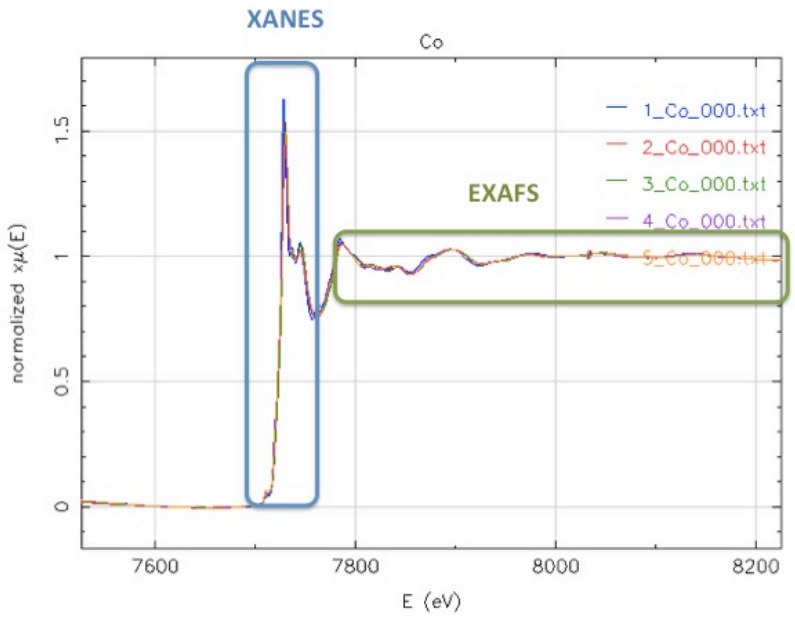

Fig. 9 Normalized XAFS μ(E) for Co with XANES and EXAFS region identified.

3.2 EXAFS

In this chapter, basic principles of EXAFS together with the presentation of EXAFS equation will be demonstrated. We focus on a physical description of the EXAFS process and a qualitative representation of the different parameters affecting the fine structure.

When X-ray is absorbed by a core-level electron, a photoelectron with wave number k is created and propagates away from the atom. In the case where a neighboring atom is introduced, the photoelectron can scatter from the electrons of this neighboring atom and return to the absorbing atom. The scattering of the outgoing electron-wave from the neighbouring atoms affects the amplitude of the photoelectron, which eventually results in the oscillation of the linear absorption coefficient with changing incident x-ray energy (Fig. 10). From this qualitative picture an expression to calculate the EXAFS can be developed.

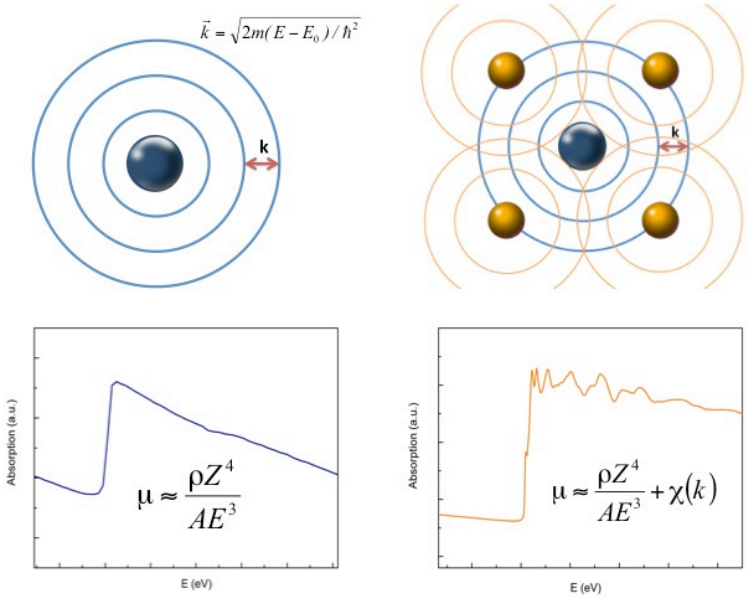

Fig. 10 Scheme of EXAFS principles. [28]

The total absorption coefficient μ can be expressed as the isolated atomic absorption μ_0 times a correction factor χ, which is also defined as EXAFS structural signal.

$$\mu(E) = \mu_0(E)[1 + \chi(E)] \tag{5}$$

or

$$\chi = [(\mu(E) - \mu_0(E)]/\mu_0(E) \tag{6}$$

For practical purpose, the denominator is often replaced by $\mu_0(E_0)$ which is the atomic absorption evaluated at the edge energy. χ can be considered as the fractional change in absorption coefficient induced by the presence of neighboring atoms.

Conventionally, the EXAFS oscillations are often defined with respect to the photoelectron wave number k.

$$k = \sqrt{\frac{2m}{\hbar^2}(\hbar\omega - E_0)} \tag{7}$$

where E_0 is the binding energy of the core-electron that is excited and $E = \hbar\omega$ is the energy of the absorbed x-ray photon.

The outgoing photoelectron can be described by a travelling spherical wave with wavenumber k and an amplitude which is proportional to $r^{-1}\exp(ikr)$. The outgoing photoelectron wave-function can be described as:

$$\psi(k,r) = \frac{e^{ikr}}{kr} \tag{8}$$

The neighbouring atoms scatter the incoming wave into a new spherical wave and this wave is proportional to the amplitude of the incident wave and the backscattering amplitude f(k), which is dependent on the type of backscatterer. Considering the backscattered wave emanating from R, detected amplitude at the origin (R=0) is proportional to $f(k)\exp(i2kR)/R^2$.

As the electron is not moving in a constant potential, a phase shift δ(k) has to be added to this expression to account for the interaction of the electron with the varying potential of the absorber atom and of the backscattering atom. It must be distinguished between the phase shift of the absorbing atom $\delta_a(k)$ and the backscattering atom $\delta_b(k)$. δ(k) is the sum of both phase shifts, but the phase shift of the absorber atom $\delta_a(k)$ has to be counted twice in this sum, hence $\delta(k) = 2\delta_a(k) - l\pi + \delta_b(k)$, where l = 1 for K edges according to the dipole selection rules. Thus we obtain the equation for the EXAFS χ(k):

$$\chi(k) \propto \frac{e^{ikR}}{kR}[2kf(k)e^{i\delta(k)}]\frac{e^{ikR}}{kR} + c.c \tag{9}$$

Note that f(k) is characteristic of the backscattering atom while the phase shift δ(k) is the sum of two independent functions associated with photoabsorber and backscatterer atoms, respectively. This fact is at the basis of the standard EXAFS data analysis method.

This also explains the sensitivity of EXAFS signal to the atomic species of the neighboring atoms. The equation can be simplified to:

$$\chi(k) = f(k)\frac{sin[2kR + \delta(k)]}{2kR^2} \tag{10}$$

The treatment here describes the scattered signal from a single atom at a distance R. In condensed matter the absorber atom has in general more than one next nearest neighbours and therefore, the equation must be summed over the scattering contribution of all neighbours. Atoms at the same radial distance and of the same

element contribute to the same components of the EXAFS signal. This group of atoms is called a coordination shell. But even the distance between the absorber and the backscatterers in one shell might not be identical due to structural disorder and atom vibrations brought by thermal excitations. Thus the contributions from atoms in one shell will not be exactly in phase. If the disorder is small and has a Gaussian distribution around the average distance R, the dephasing can be taken into account by a damping factor $\exp(-2k^2\sigma_j^2)$ and $\sigma_j^2 = \langle[\vec{r_j} \cdot (\overrightarrow{u_j} - \overrightarrow{u_0})]^2\rangle$ is the mean-square-average of the difference of displacements $(\overrightarrow{u_j} - \overrightarrow{u_0})$ of the backscatter j and the absorber along the equilibrium bond direction $\vec{r_j}$. The term σ_j^2 is often referred to as EXAFS Debye-Waller factor. This disorder will thus change the EXAFS equation to:

$$\chi(k) = \frac{Ne^{-2k^2\sigma^2} f(k)}{2kR^2} sin[2kR + \delta(k)] \tag{11}$$

Where N is the coordination number. It is to be noted that only the vibrations relative to the absorbing atom are taken into account and for example long wavelength photons will not contribute to the EXAFS Debye-Waller factor, since the two atoms (absorber and backscatterer) are too close to each other and their contribution to the difference of displacements $(\overrightarrow{u_j} - \overrightarrow{u_0})$ is negligible.

Real systems usually have more than one type of neighboring atom around the absorbing atom. This can be easily accommodated in the XAFS formula since the measured EXAFS signal will simply be a sum of the contribution from each scattering path:

$$\chi(k) = \sum_j \frac{N_j e^{-2k^2\sigma_j^2} f_j(k)}{2kR_j^{\,2}} sin[2kR_j + \delta_j(k)] \tag{12}$$

where j represents the individual coordination shell of identical atoms at approximately the same distance from the central atom. In some cases when the shells of similar Z are close enough (*i.e.*, within 0.05Å of each other), they become difficult to distinguish from one another.

The last effect that has to be taken into account is the lifetime τ_0 of the excited photoelectron states and on the lifetime of the photoelectron itself. In order to be detected in EXAFS, the photoelectron has to be scattered from the neighbouring atom and return to the absorbing atom elastically. When we asserted that the outgoing photoelectron went out as a spherical wave, we neglected the fact that the

photoelectron can also scatter inelastically from other sources (other conduction electrons, phone *etc*.). In addition, the photoelectron has to make it back to the absorbing atom before the core hole is filled by another electron. To account for both the inelastic scattering and the core-hole lifetime, we use a damped spherical wave:

$$\psi = \frac{e^{ikr}e^{-2r/\lambda(l)}}{kr} \tag{13}$$

where λ(k) is called the mean free path of the photoelectron (*i.e*., how far it typically travels before scattering inelastically and before the core-hole is filled). The mean free path has a significant but fairly universal dependence on k. Usually it is expected that shells, which are further apart than 10Å from the absorber, are not visible in the spectrum. So finally the following expression is obtained to describe the EXAFS oscillations χ(k).

$$\chi(k) = \sum_j \frac{N_j S_0^2 f_j(k) e^{-2R_j/\lambda(k)} e^{-2k^2\sigma^2}}{2kR_j^2} sin[2kR_j + \delta_j(k)] \tag{14}$$

The amplitude reduction term S_0^2 accounts for shake-up /shake-off processes of the central atom. Those processes (multi-excitations) refer to the excitations of the remaining Z-1 "passive" electrons of the excited atom. Although S_0^2 is weakly energy dependent, it is usually approximated by a constant. The amplitude reduction term differs for different elements and the values range from $0.6 < S_0^2 < 1.0$.

Key approximations of this equation include: plane wave approximation, K threshold, single scattering, single electron approximation, and "sudden" approximation.
From this equation, a few physical conclusions can be drawn about EXAFS. First, because of the λ(k) and the R^{-2} term, EXAFS is seen to be an inherently local probe, not able to see much further than 5Å or so from the absorbing atom. Second, the EXAFS oscillations will consist of different frequencies that correspond to the different distances for each coordination shell, which will require the use of Fourier Transforms in the data processing. Finally, in order to extract the distances and coordination numbers, we need to have accurate values for the scattering amplitude f(k) and phase-shift δ(k).

3.3 XANES

Absorption edge by itself is of little value beyond elemental identification. However, a close-up examination of the absorption profile will reveal a wealth of information

about the geometric and electronic structure. Strictly speaking, XANES also includes several weak transitions below the edge, referred to as pre-edge peak, which is brought up by electronic transitions. Sometimes a sharp intense peak called white lines can also be observed on the rising edge. The reason is that in the past, X-ray absorption spectra were recorded using photographic plates, and the strong absorption of certain wavelength leads to an unexposed band on the photographic plates which after develops in negative, appear as a white vertical stripe, hence the term "white line". Above the edge, there are a variety of structures that show generally oscillatory behavior, ultimately becoming the EXAFS oscillations. Fig. 11 shows an expansion of XANES region.

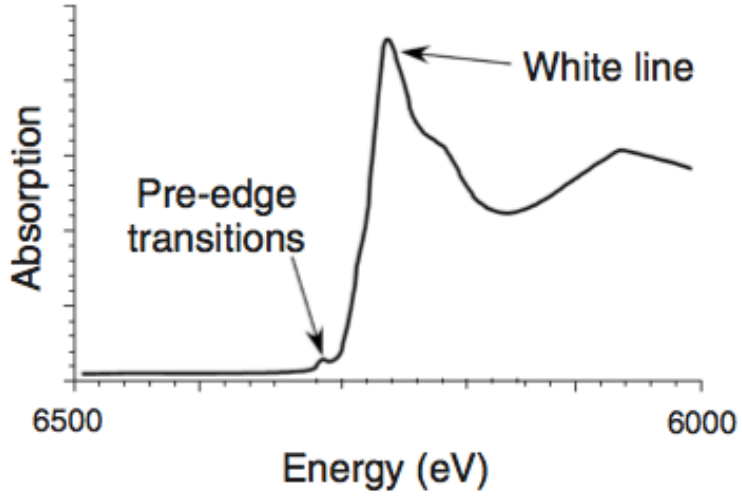

Fig. 11 Expansion of XANES region with different features.

Although the same physical principles govern both the EXAFS and the XANES region, however, in the region close to threshold, photoelectron has low kinetic energy, giving it a long mean free path. These effects combine to make the XANES region sensitive to longer distance absorber-scatter interaction than are typically sampled by EXAFS. This greatly complicates simulation of XANES structure, since many interactions and a large number of multiple scattering pathways need to be included. However, the sensitivity to multiple scattering is, at least in principle, an advantage since it provides the possibility of extracting information about three-dimensional structure from XANES spectra.

Although much progress has been made recently in the theoretical modeling of XANES, the quantitative accuracy of its calculation is yet to be improved. Nevertheless, it could be of importance to make even qualitative fingerprint-like

comparisons of XANES spectra. If a representative library of reference spectra is available, spectral matching can be used to identify an unknown structure. Beyond this qualitative application, there are three main ways in which XANES spectra are used: to determine oxidation state, to deduce three-dimensional structure, and as a probe of electronic structure.

The weak transitions in the pre-edge region arise from bound state electronic transitions and are normally observed for transition metal with an open d shell. They present as "weak" transitions compared with the intense edge jump since they are theoretically forbidden by dipole selection rules. Nevertheless, the 1s-3d transition gains intensity through both 3d-4p mixing and direct quadrupolar coupling. Peak intensity is believed to increase as the site is distorted from its centrosymmetric environment (*i.e.*, $I_{octahedral} < I_{square\text{-}pyramidal} < I_{tetrahedral}$), whilst molecules with high centrosymmetry have relatively low intensity (*i.e.*, square-planar). The pre-edge sensitivity to 3d-4p mixing indicates its application as a probe of geometry to explore the electronic structure of the absorbing atom.

The pre-edge also contains information about oxidation state with the same principle as edge step to be explained in the following chapter. Higher oxidation of the metal leads to greater stabilization of the 1s orbital with respect to the metal d orbitals, thus, leading to higher energy of the pre-edge.

The energy of an absorption edge is not well defined. It can be taken as the energy at half-height or more commonly, as the maximum of the first derivative with respect to energy. However, as shown by Fig. 11, edge spectra frequently have unresolved transitions superimposed on the rising edge. These will affect any attempt to define a unique "edge energy". Despite this ambiguity, edge energies have proven extremely useful in determining the oxidation state of the absorber. It has been known for many years that the energy of an edge increases as the oxidation state of the absorber increases. This can be explained using an electrostatic model, since atoms with a higher oxidation state should have a higher charge, thus requiring more energetic X-ray to eject a core electron. An alternative interpretation of edge energies treats the edge features as "continuum resonances". A continuum resonance involves excitation of a core electron into a high-energy state (above the continuum) that has a finite lifetime. An example is the potential well created by the absorbing and scattering (nearest neighbor) atoms. As the absorber–scatterer distance gets shorter, the energy of the continuum state increases as $1/R^2$. Since higher oxidation state metals have shorter bond lengths, both models predict an increase in edge energetic with increasing oxidation state. Regardless of which explanation is most appropriate, the correlation between edge energy and oxidation state is well

established and widely used in coordination chemistry.

As noted above, multiple scattering is particularly important in the XANES region. In principle, this means that it should be possible to determine the three-dimensional structure of the absorbing atom from analysis of the XANES features. Empirically, this is certainly the case; the XANES region is quite sensitive to small variations in structure, to the extent that two sites having identical EXAFS spectra can nevertheless have distinct XANES spectra. This sensitivity is, at least in part, due to the fact that geometrical differences between sites alter the multiple scattering pathways, and thus the detailed structure in the immediate vicinity of the absorption edge. Although there has been progress in the interpretation of XANES spectra, the agreement between calculated and observed spectra remains relatively poor in most cases. The development of theoretical and computational methods that will permit detailed interpretation of XANES spectra is one of the outstanding problems in the field.

4. Experimental Part

4.1 Electrochemical Testing

Material synthesis has been done at the University of Munster by group of Prof. Passerini. The preparation of the electrodes for the ex-situ measurements is as follows: 10 pallets of Li-half cell were prepared (d=13mm) and cycled with C/10 (20 mA/g) to a certain potential, *e.g.*, certain capacity. The cells were then rested for a fixed amount of time before open circuit voltage (OCV) of each cell was checked. Afterwards they were disassembled; the electrodes were washed with DMC, dried and sealed in PE or PP foil.

Fig. 12 shows the voltage profile of the cell during charge-discharge. The numbered points alone the curves indicate predetermined states of charge at which cells were prepared for the XAS measurements. Point 1 represents the fresh, unchanged electrode, point 2 to 4 corresponds to the extraction of ~83, 103, 200mAh/g capacity, and point 5 represents a fully charged electrode at 4.8V corresponding to the full ~347mAh/g practical capacity of the electrode. Point 8 represents a fully discharged electrode at 2.6V after one complete cycle. Point 9 and 10 were taken on the second charge process.

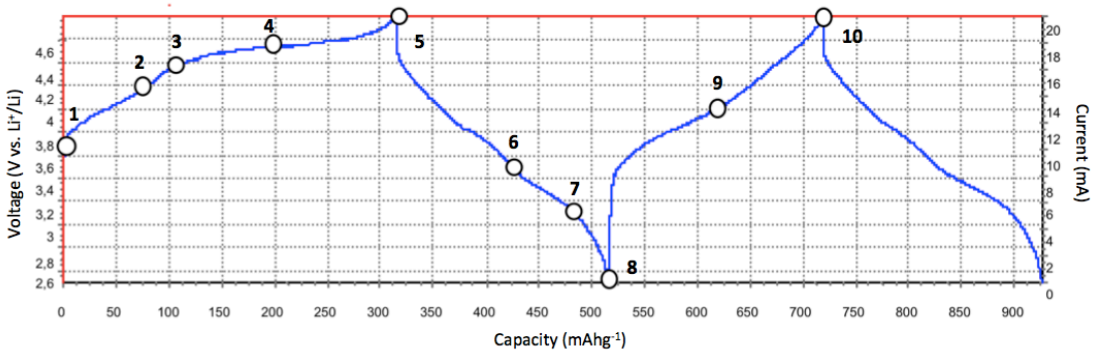

Fig. 12 Voltage profile of the charge and discharge circles of Li-rich NCM (C/10 rate, 20mA/g). Representative points of 1-10 in the process of XAS measurements are indicated.

Reaction formula during charge at the cathode can be written as (discharge reaction the other way around):

$$Li_{1.2}Mn_{0.56}Ni_{0.16}Co_{0.08}O_2 - xe^- \xrightarrow{charge} Li_{1.2-x}Mn_{0.56}Ni_{0.16}Co_{0.08}O_2 + xLi^+$$

And at the anode:

$$C_6 + xLi^+ + xe^- \xrightarrow{charge} C_6Li_x$$

	Composition	Mass Loading (mg/cm^2)	Capacity (mAh/g)	Voltage (V)	OCV (V)
1	$Li_{1.2}Mn_{0.56}Ni_{0.16}Co_{0.08}O_2$	4.37	0	3.7	3.70
2	$Li_{0.94}Mn_{0.56}Ni_{0.16}Co_{0.08}O_2$	4.37	83	4.2	4.14
3	$Li_{0.86}Mn_{0.56}Ni_{0.16}Co_{0.08}O_2$	4.52	103	4.4	4.26
4	$Li_{0.55}Mn_{0.56}Ni_{0.16}Co_{0.08}O_2$	4.45	200	4.5	4.29
5	$Li_{0.16}Mn_{0.56}Ni_{0.16}Co_{0.08}O_2$	4.12	347	4.8	4.35
6	$Li_{0.45}Mn_{0.56}Ni_{0.16}Co_{0.08}O_2$	3.93	103	3.7	3.78
7	$Li_{0.72}Mn_{0.56}Ni_{0.16}Co_{0.08}O_2$	4.26	180	3.4	3.48
8	$Li_{0.89}Mn_{0.56}Ni_{0.16}Co_{0.08}O_2$	4.23	238	2.5	3.22
9	$Li_{0.59}Mn_{0.56}Ni_{0.16}Co_{0.08}O_2$	4.07	103	3.9	3.82
10	$Li_{0.02}Mn_{0.56}Ni_{0.16}Co_{0.08}O_2$	4.90	245	4.8	4.41

Tab. 1 Measured data of sample parameters at different stages of charge-discharge, namely mass loading, capacity, voltage and open circuit voltage. Composition of samples during cycling are calculated with mass loading and corresponding capacity, assuming that all charges are consumed by the Li extraction/insertion without any side reactions, *e.g.*, electrolyte decomposition.

4.2 Synchrotron Radiation Experiment

X-Ray Absorption Spectroscopy (XAS) spectra have been recorded at ELETTRA Synchrotron Radiation Laboratory (Basovizza, Italy), through the project # 20110095 "X-Ray Absorption Spectroscopy Structural Studies on High Voltage Cathode Materials of the $Li[Li_{0.2}Mn_{0.6-0.5x}Ni_{0.2-0.5x}Co_x]O_2$ family" (project leader M. Giorgetti). The storage ring was operated at 2.0 GeV in top up mode with a typical current of 300 mA. The data were recorded at Mn K-edge (6539 eV), Co K-edge (7709 eV) and Ni K-edge (8333 eV) in transmission mode using ionization chamber filled with a mixture of Ar, N_2 and He in order to have 10%, 70% and 95% of absorption in the I_0, I_1 and I_2 chambers, respectively. Pellets for transmission measurements (13mm diameter) were prepared by mixing powder samples with cellulose, with mass loading of active material of about 3-4 mg/cm^2, which ensures a suitable absorption edge for the three threshold simultaneously. The white beam was

monochromatized using a fixed exit monochromator equipped with a pair of Si (111) crystals. Harmonics were rejected by using the cutoff of the reflectivity of the Platinum mirror placed at 3 mrad with respect to the beam upstream the monochromator and by detuning the second crystal of the monochromator by 30%. Internal reference of Mn, Co, and Ni foil were used for energy calibration in each scan. This allowed a continuous monitoring of the energy during consecutive scans. Therefore, energies were defined by assigning to 6539, 7709 and 8333 eV the first inflection point of the spectrum of the Mn foil, Co foil and Ni foil, respectively. No energy drifts of the monochromator were observed during the experiments. Spectra were collected with a constant k-step of 0.03 Ang.-1 with 3s/point acquisition time from 6330 to 7700eV (Mn K-edge); from 7550 to 8320eV (Co K-edge) and from 8150 to 9500eV (Ni K-edge).

4.3 Pre-processing by Athena

XAS spectra of 10 Li-rich NCM samples taken at ten different stages of the first two charge-discharge circles are provided.

Edge position E_0 of each spectrum was selected by using the zero crossing of the second derivative of μ(E) in the "Data Calibration" dialogue from the "Data" menu. The first maximum of the first derivative introduces errors when peaks with flat tops or fake spikes appear in some cases. Care should be taken to check both derivative spectra to ensure selection of the right inflection, making sure that edge energy shifts vary within 4eV for each element.

Energy calibration is necessary since absorption energy of reference Co, Mn and Ni foil appears different from tabulated value. The reference of a first scan of each element was calibrated and put at its proper place on an absolute energy scale. Then each of the reference channels was aligned to the reference channel of the designated standard. In many cases, following this procedure and trusting the automated alignment is sufficient to prepare the data for further analysis. In this version of Athena software, energy shifts for the sample are displayed automatically according to the corresponding reference value but manual modification of the edge energy is needed to ensure that they fluctuate around the tabulated value.

A standard edge step normalization was performed on all spectra in removal of variations in sample and detector setup. Pre-edge and normalization range were carefully adjusted to ensure that both pre-edge and post-edge lines pass through the middle of the data in their respective ranges (visual inspection is more than enough in this case). Deglitching, truncating and smoothing were not performed thanks to

the relatively good data quality. Normalization order was set at 3 and normalized data were flattened by default.

In the “Background removal” tab of the Athena software, the Rbkg parameters were set at 1.2, 0.9 and 1 respectively for Co, Mn and Ni based on the best suppression outcome of the low-R peaks. Comparison of this value with half the distance to the nearest neighbor (available from crystallographic data) is needed for further confirmation of the optimized Rbkg value. K-weight and Spline range were set according to default.

The normalized data were exported from Athena into Origin for XANES analysis including pre-edge as well as edge area. EXAFS data analysis has been done with GNXAS package on raw data.

5. Result and Discussion

5.1 Structure of $Li[Li_{0.2}Mn_{0.56}Ni_{0.16}Co_{0.08}]O_2$

As elaborated in the introduction part, our Li-rich cathode material crystallize in a layered structure which can be classified as α-$NaFeO_2$ type rock salt, consisting of close-packed network of oxygen atoms with lithium layers and layers containing the transition metal ions, namely Ni^{4+}, Ni^{2+} and Co^{3+}. The lithium ions are at the 3a sites and the metal ions are at the 3b sites in a hexagonal setting of the $R\bar{3}m$ space group. Oxygen is reported to be at the 6c lattice position. Atomic occupancy of different sites can be denoted as $[Li]_{3a}[M]_{2b}[O2]_{3c}$. Note that a certain degree of "caution mixing" (*i.e.*, Li in 3b sites and transition metal in 3a sites) are reported in all similar compounds by X-ray Diffraction analysis [29] that often lead to structural disordering, and moreover, degradation of electrochemical performance during cycling.

5.2 XANES Analysis: edge jump

5.2.1 Energy Calibration

For the XAFS analysis, reference samples that remains unchanged for the duration of the experiment need to be recorded to monitor energy calibration. If the energy of the monochromator output beam varies, this will be detected as a shift in the position of the edge of the reference sample, which can be used to compensate for such shifts. In this case, reference spectra for each element exhibit great alignment for the duration of the ten measurements, which ensure the stability of monochromators (Fig. 13).

(a)

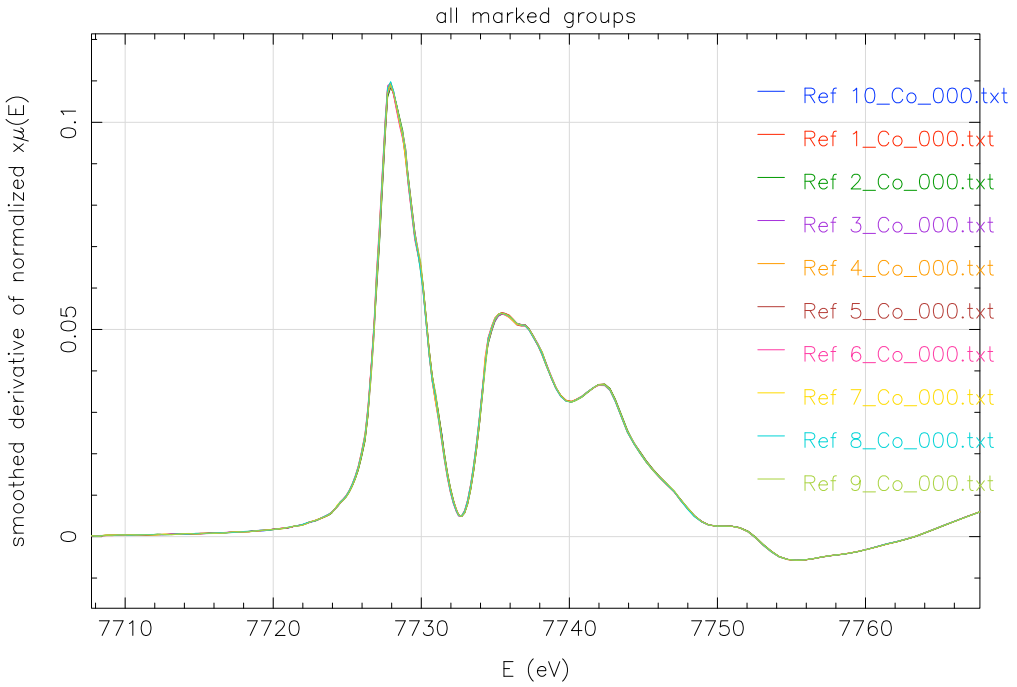
all marked groups
smoothed derivative of normalized xμ(E)
0
0.05
0.1
7710
7720
7730
7740
7750
7760
E (eV)
Ref 10_Co_000.txt
Ref 1_Co_000.txt
Ref 2_Co_000.txt
Ref 3_Co_000.txt
Ref 4_Co_000.txt
Ref 5_Co_000.txt
Ref 6_Co_000.txt
Ref 7_Co_000.txt
Ref 8_Co_000.txt
Ref 9_Co_000.txt

(b)

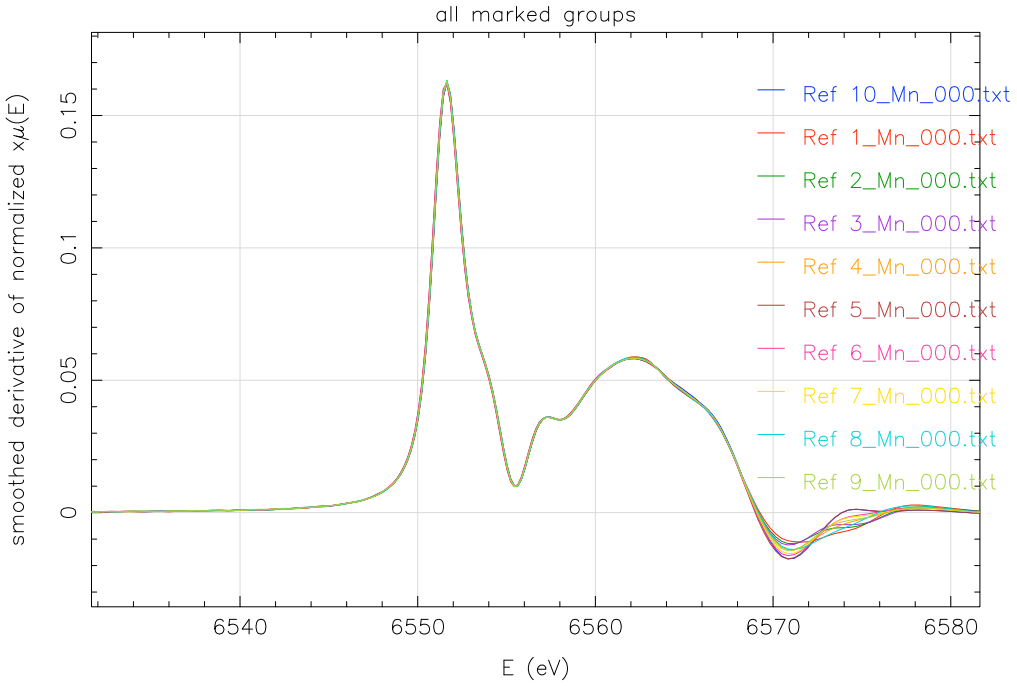
all marked groups
smoothed derivative of normalized xμ(E)
0
0.05
0.1
0.15
6540
6550
6560
6570
6580
E (eV)
Ref 10_Mn_000.txt
Ref 1_Mn_000.txt
Ref 2_Mn_000.txt
Ref 3_Mn_000.txt
Ref 4_Mn_000.txt
Ref 5_Mn_000.txt
Ref 6_Mn_000.txt
Ref 7_Mn_000.txt
Ref 8_Mn_000.txt
Ref 9_Mn_000.txt

(c)

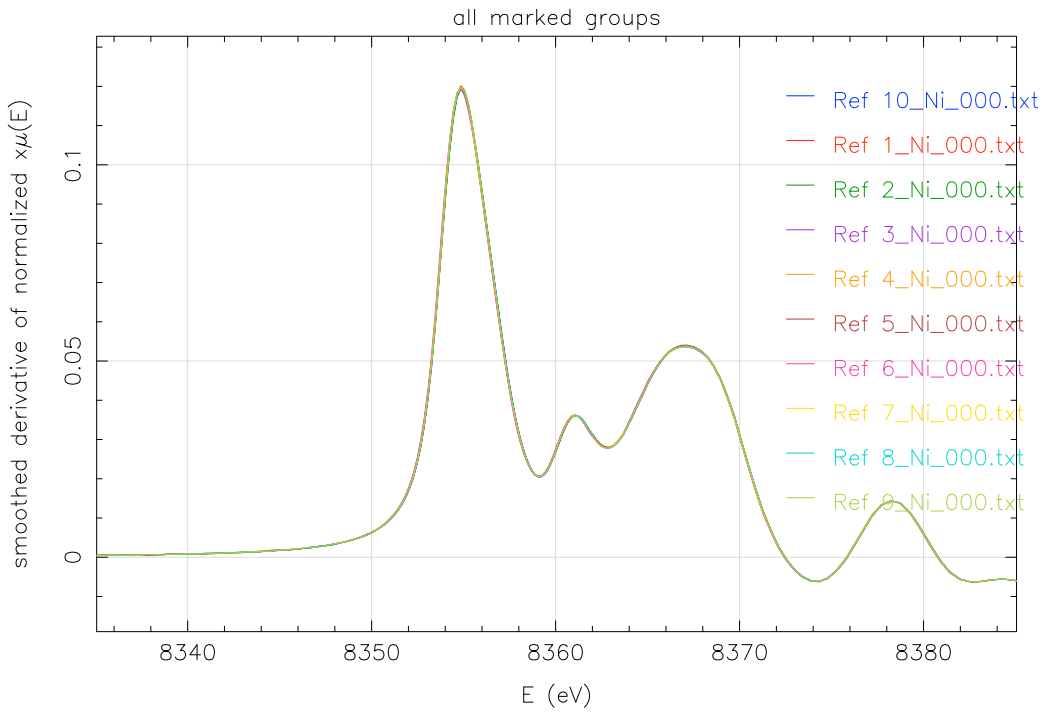

Fig. 13 Derivative of normalized EXAFS reference spectra of (a) Co, (b) Mn, and (c) Ni, processed by ATHENA.

5.2.2 Discussion

Normalized XANES spectra of the 10 investigated cathodes are presented in Fig. 14 for the Mn K-edge (a), Co K-edge (b) and Ni K-edge (c), respectively. All spectra are characterized by a pre-edge peak A, a bound B in the rising part of the edge and a main peak C. The general accepted assignment of these peaks are: 1) Peak A is due to 1s-3d electron transition, the details and analysis of which will be presented in the next section; 2) Peak B is assigned to 1s-4p transitions plus a shakedown process caused by ligand-to-metal charge transfer; 3) Peak C is a pure 1s-4p dipole allowed transition.

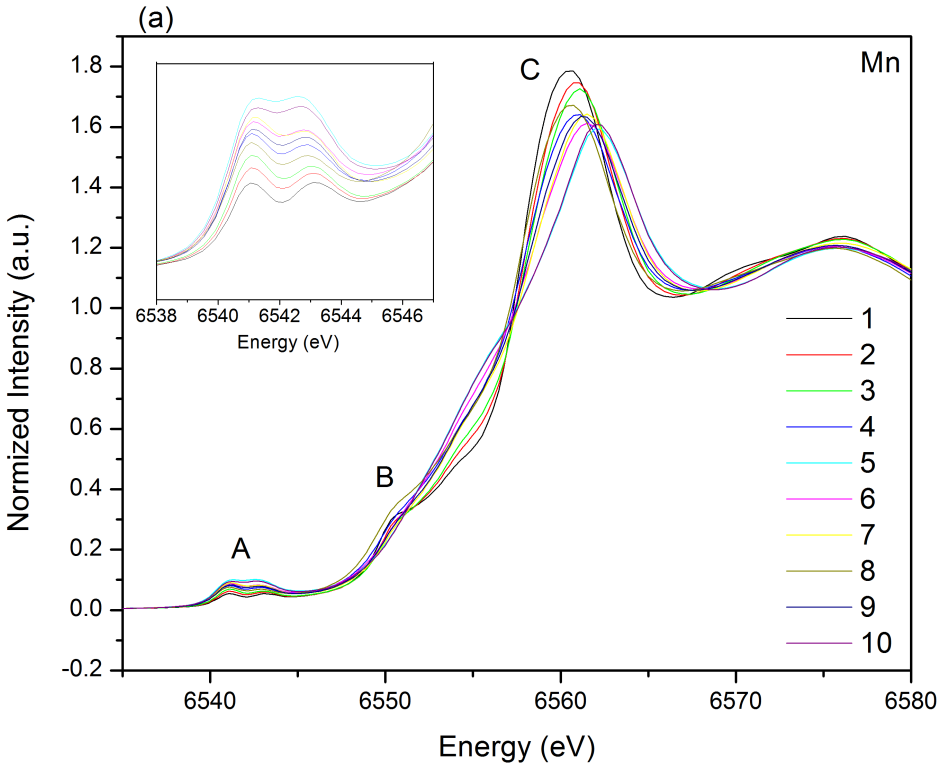
(a)
Mn
C
B
A
Normized Intensity (a.u.)
Energy (eV)
6538 6540 6542 6544 6546
Energy (eV)
1
2
3
4
5
6
7
8
9
10

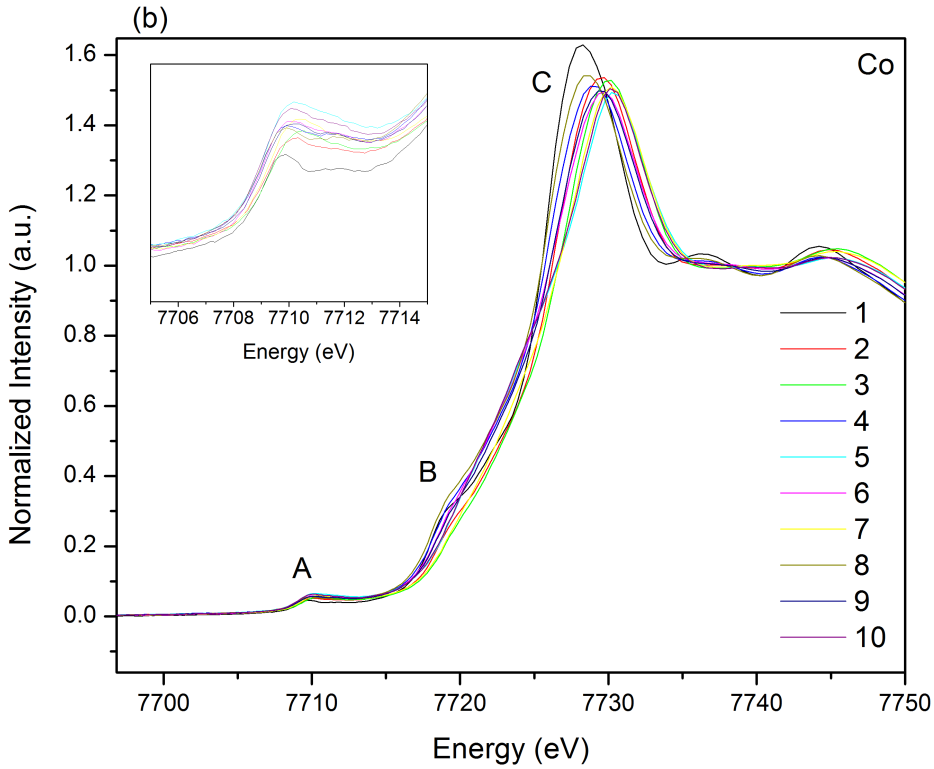
(b)
Co
C
B
A
Normalized Intensity (a.u.)
Energy (eV)
7706 7708 7710 7712 7714
Energy (eV)
1
2
3
4
5
6
7
8
9
10

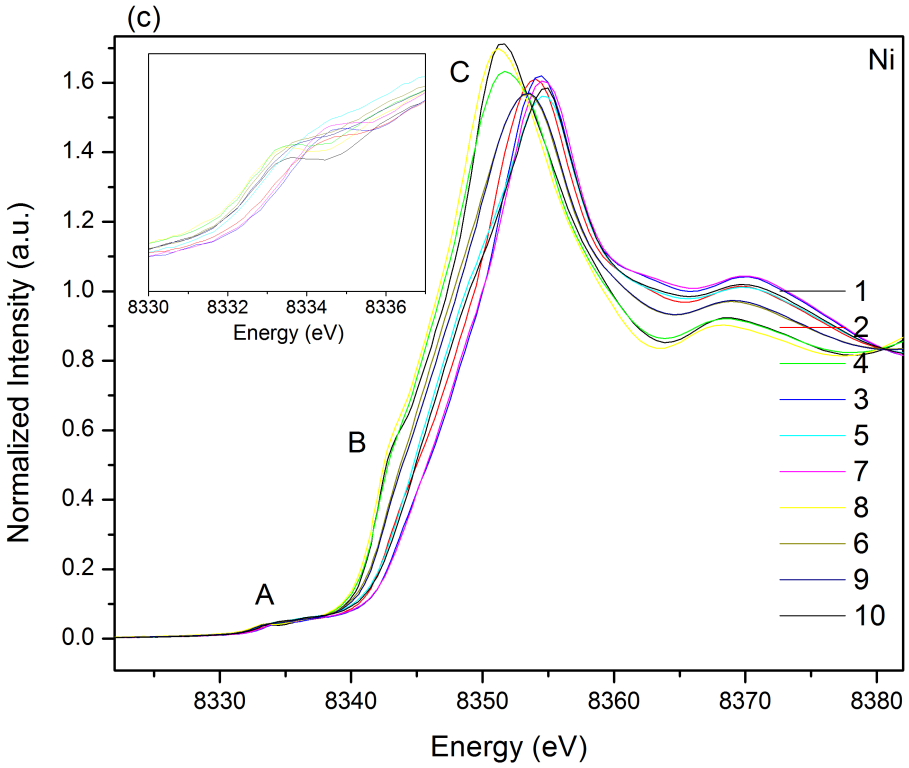

Fig. 14 Normalized K-edge XANES spectra at different stages of charge-discharge collected at (a) Mn K-edge, (b) Co K-edge, and (c) Ni K-edge with an inset graph of the zoom-in of the pre-edge region.

The energy of the recorded spectra is certainly related to the valent states of the center atom. Spectra profile provides information about site symmetry and the nature of bonding with surrounding ligands, [30] for example, modification of local structures. It can also be influenced by change in electronic structure of the probed metal without change in oxidation state. In several cases care should be taken in charge analysis due to the changes in edge features. In the case of Mn in Fig. 14 (a), the XANES spectrum exhibits some changes in the slope and the edge due to variations of local environment and it does not show an progressive shift to higher energy value. Thus using edge energy to determine Mn valence change might induce ambiguity. Therefore, this study will focus on the use of pre-edge energy in examining variations in valent states.

The edge positions for all measurements are indicated in Tab. 2. The shift of edge positions for Mn is not obvious with a slight increment during charge and reduction during discharge. A comparison of the K-edge of Mn pristine sample with model

compounds Li_2MnO_3 (Mn^{4+}) can be seen in Fig. 15. Their difference in edge energy is calculated to be 0.2eV indicating the tetravalent state of Mn in the cathode sample. This is a typical example of determining oxidation state of samples at different state of charge-discharge in utilization of the "fingerprint" characteristic of XANES data. Considering the fact that pre-edge energies for Mn remain invariant during change-discharge, we can safely deduce that the oxidation state of Mn remains as +4 throughout the cycling process and does not take part in redox reactions in the following cycling.

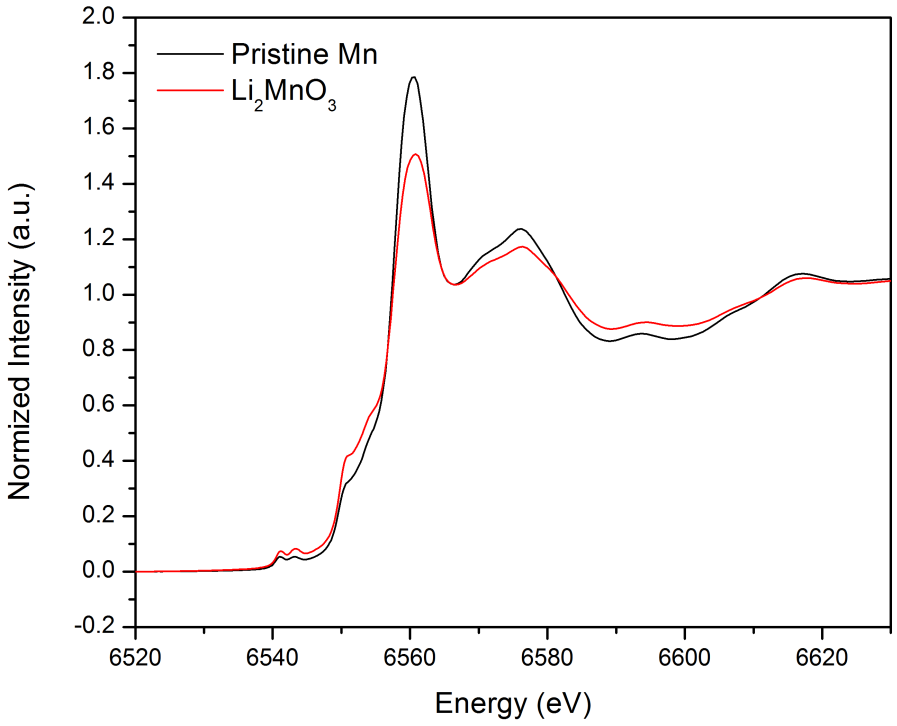

Fig. 15 Normalized XANES comparison of pristine sample at Mn K-edge with model compound Li_2MnO_3 (Mn^{4+}).

Note that a "Mn activation" process where have been reported in similar compounds $Li_{1.2}Mn_{0.54}Ni_{0.13}Co_{0.13}O_2$ (or 0.5 Li_2MnO_3-0.5$Mn_{1/3}Ni_{1/3}CoO_2$) (2) as well as pour Li_2MnO_3 [31] where Mn ions become redox active species after charging up to 4.8eV during initial charge. But this phenomenon is not observed in our cathode material, neither in $Li[Li_{1/9}Mn_{5/9}Ni_{1/3}]O_2$. Possible explanation is the content of Li_2MnO_3 component, which is closely correlated with the amount of oxygen removed and structural rearrangement.

In contrast, the Ni K-edge of Fig. 14 (c) shifts to higher energy values during charging with an increment of around 2.5eV. This suggests that the average oxidation state of nickel ion increases during charge, and hence the large shifts can be correlated to Ni^{2+}/Ni^{4+} oxidation, more precisely, oxidation from a mix state of $Ni^{2+/3+}$ to $Ni^{3+/4+}$ as suggested by research on Li-excess materials. [32] Sample 4 behaves differently, as it appears smaller in terms of energy as regard to Sample 1 and thus a possible reduction mechanism of Ni^{4+} to Ni^{2+} can be proposed. This aspect will be analyzed further in the general discussion section.

Co K-edge of Fig. 14 (b) is in the intermediate situation. It possesses similar energy shift as Ni, but barely detectable because of the presence of changes in the edge feature as observed in the case of Mn.

	Co (eV)	**Mn (eV)**	**Ni (eV)**
1	7725.9	6557.8	8349.4
2	7726.3	6557.9	8350.9
3	7727.4	6558.0	8351.2
4	7725.9	6558.0	8348.8
5	7728.3	6560.4	8352.2
6	7726.4	6558.6	8349.7
7	7727.7	6558.0	8352.3
8	7725.9	6557.7	8348.7
9	7726.3	6558.0	8349.7
10	7728.1	6560.4	8352.6

Tab. 2 Edge positions (in eV) for the Co, Mn and Ni K-edge XANES during charge-discharge.

5.3 XANES Analysis: pre-edge

5.3.1 Origin Pre-processing

Only segments of the data in the pre-edge range were retained for pre-edge analysis (Co: 7720-7736eV, Mn: 6546-6559eV, Ni: 8350-8360eV). Origin failed to perform a reasonable background subtraction for the whole spectrum without loosing the pre-edge characteristics. Peak fitting was made possible by the Origin "Peak Analyzer" wizard. "Fit Peaks" goal was selected in the first step of peak analyzing

(function available only with Origin Pro). User defined baselines were applied then subtracted and well-fitted pre-edge peaks could be obtained with Gaussian lines. The resulting Adj. R-square values vary around 0.999 for Co, Mn and 0.998 for Ni, which proves to be satisfactory. The "Baseline Anchor Points" selection is the trickiest step and some measures were taken to minimize the errors introduced by subjective baseline point choice. For example, "Snap to Spectrum" was checked to ensure a basic selection consistency while minor changes are made in case of relative big shift of pre-edge peak. Baseline points are connected by "Spline Interpolation" instead of "Fitting" according to visual inspection. In the "Baseline Treatment" step (a dynamic wizard map of the analyzing steps can be found at the top of the dialogue which also shows the current step), "Auto Subtract Baseline" was selected as part of the final peak fits. It is to be noted that the original baseline data are not provided when this checkbox is selected, so another analysis had to be performed with the same checkbox unselected to obtain a baseline curve.

Fig. 16 shows the background subtraction process as well as peak fitting for Co, Mn and Ni pre-edge respectively. Pre-edge features were fitted by Gaussian functions after the subtraction of background.

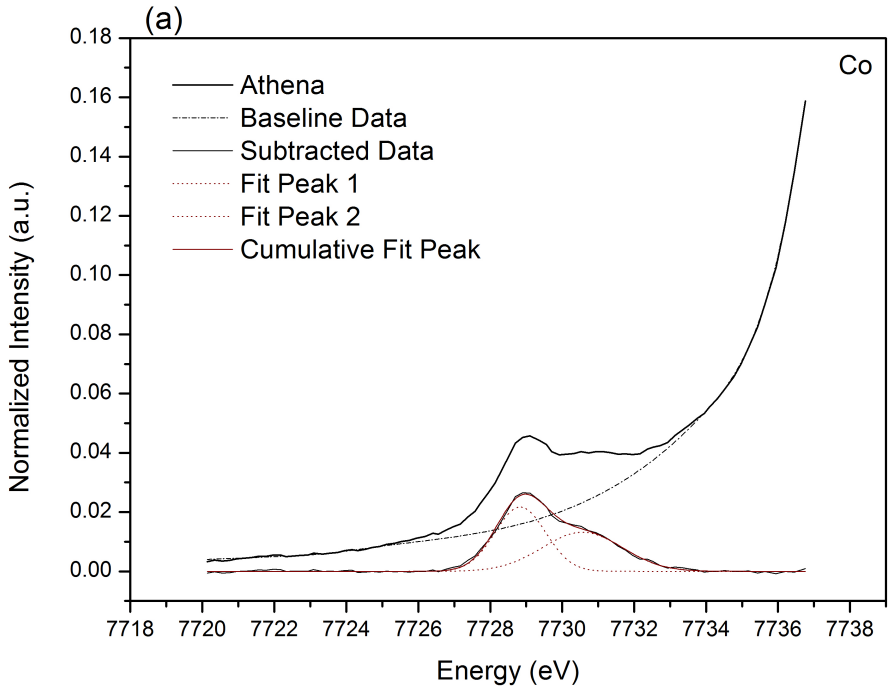

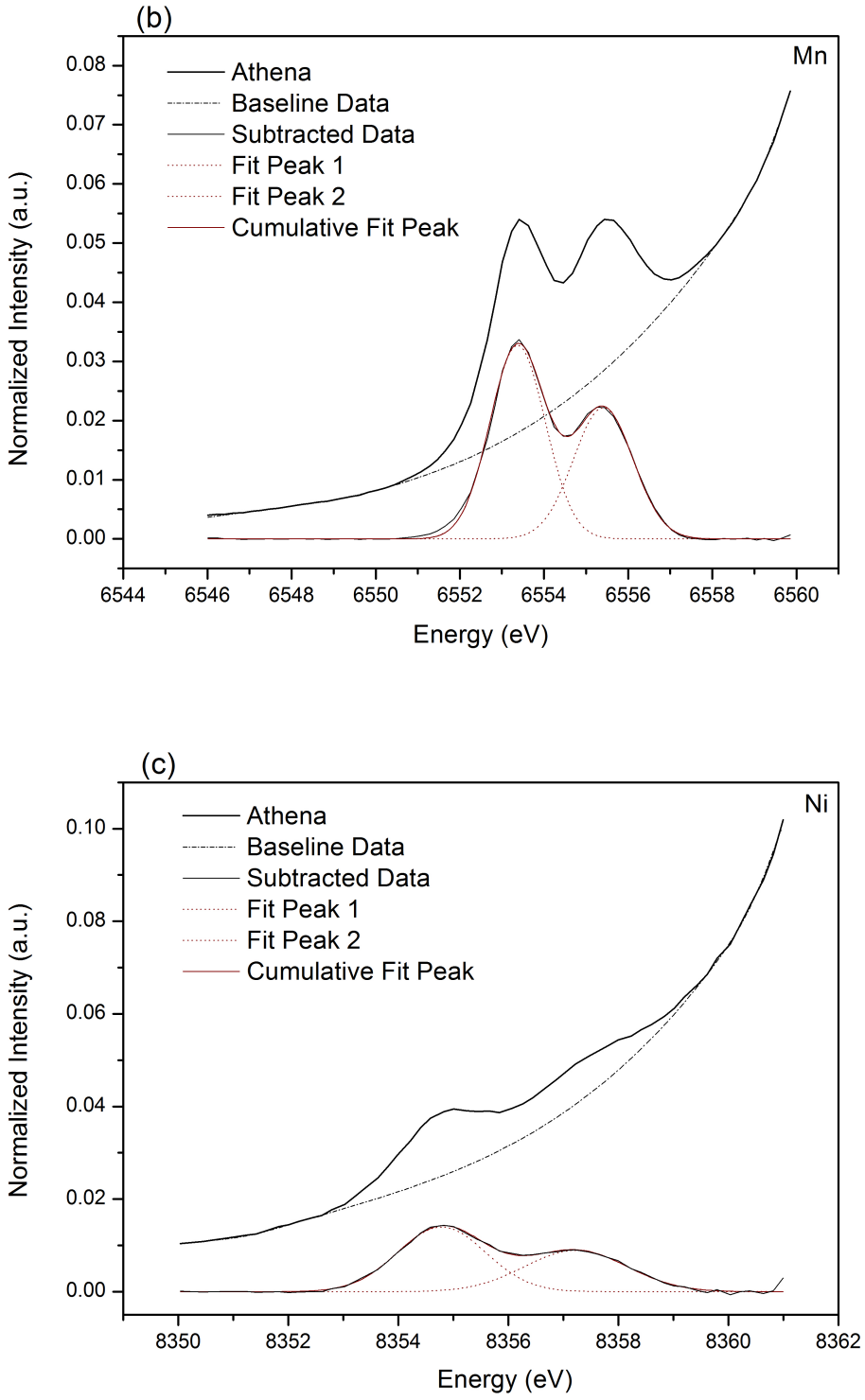

Fig. 16 Representative graphs of pre-edge background subtraction and peak fitting for (a) Co K-edge, (b) Mn K-edge and (c) Ni K-edge XANES spectra of the cathode (Before energy shifts are deducted from the original data, an energy shift of around 19eV for Co, 12eV for Mn and 21eV for Ni are considered in the following spectra).

During the pre-edge Origin pre-processing, since a "Peak Analyzer" wizard was utilized for baseline selection as well as subtraction, the pre-edge features were automatically fitted with Gaussian functions (the Adj. R-Square gives a satisfying results that amounts to 0.999), while in most references, a Voigt line shape (sum of Lorenzian and Gaussian functions) is more frequently applied. In the present case, a normal "Multiple Peak Fit" which allows manual selection of peak type could not be used in absence of a baseline subtraction function. The choice of peak type might introduce errors in the peak analysis.

It must be noted that peak areas for well-defined peaks are normally proportional to peak heights, but that this relationship breaks down, for example, in peaks which show significant broadening. In order to verify the validity of using peak heights as parameters for further analysis, area *vs*. intensity for the pre-edge peaks of Mn was plotted in Fig. 17. Mn data are selected here on account of the more apparent separation of the two pre-edge peaks, thus producing a relatively more accurate peak fitting. Simple linear fit provides an Adj. R-Square of over 0.99 for both peaks, which illustrates the successful peak fitting for the pre-edge area.

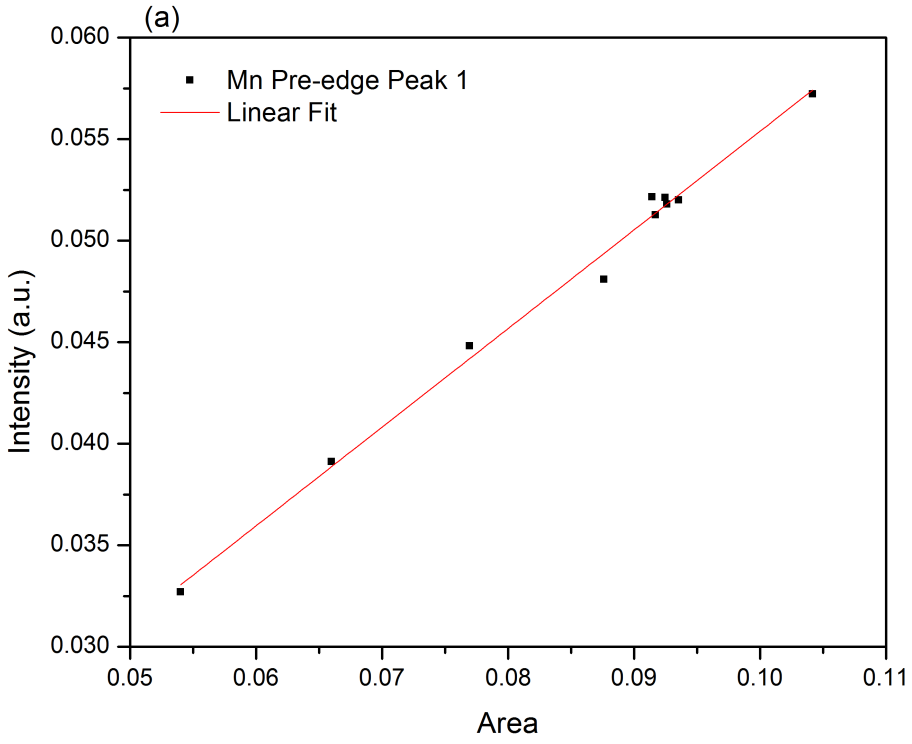

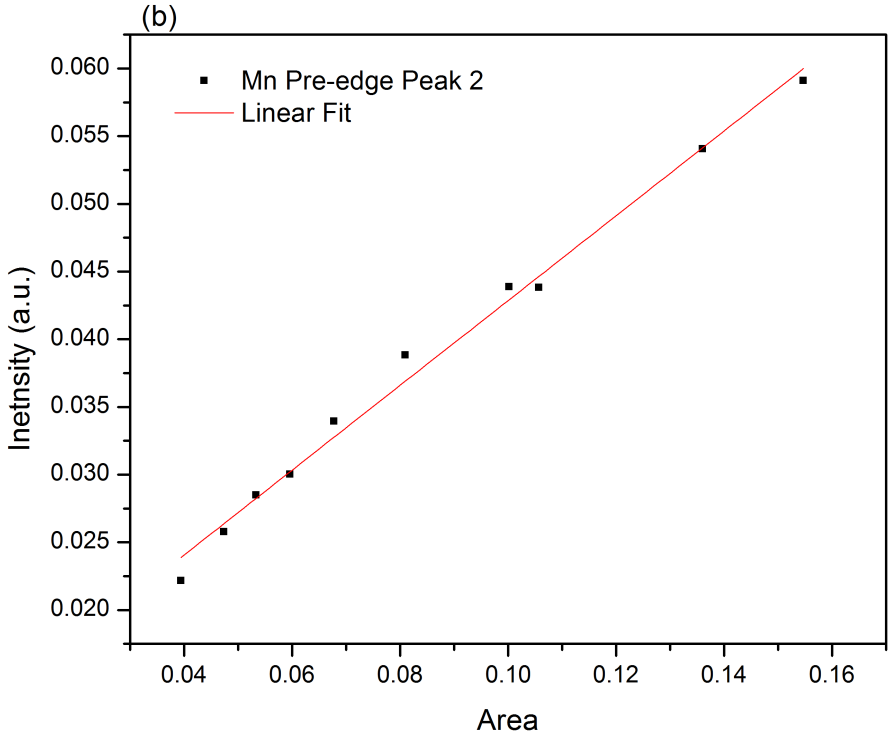

Fig. 17 Plot of the intensity of the first Mn pre-edge peaks Intensity *vs*. Area for (a) Peak 1, (b) Peak 2.

5.3.2 Discussion

Pre-edge features provide important information about electronic transitions of the material and the corresponding XANES spectra are strongly influenced by the coordination number, number of d-electrons and symmetry of the coordination sphere. [33] In this part, a general analysis of pre-edge feature will be presented in these three respects. The tendencies of each element during charge and discharge will also be discussed.

Insets of Fig. 14 shows the XANES regions of Co, Mn and Ni with a close-up exhibition of the characteristics of the pre-edge peaks. For all the three transition elements, the pre-edge peaks occur around 15eV below the absorption edge with intensity as low as <0.04 (after normalization and background subtraction). The relatively weak pre-edge intensities are assigned to transitions of a 1s electron to a 3d orbital which is directly allowed through an electric quadrupolar transition mechanism. This is a typical observation for 3d transition metals with octahedral

symmetry. The pre-edge intensity for tetrahedral species, for example, is much more intense thanks to transitions to the p component in a 4d-3p hybridized orbital since s-p transition is theoretically allowed by the selection rule while s-d transition is forbidden. But orbital hybridization does not occur with regular O_h symmetry according to group theory. Electric quadrupolar transition occurs in systems with any symmetry but its probability is quite less than that of the electric dipole transition. Blair [34] has reported that 1s-3d transition is about one thousandth of those of 1s-np transitions thus hybridization of 4p orbitals with 3d orbitals greatly enhances the pre-edge peak intensity.

In the pre-edge region for all Co/Mn/Ni, all the spectra recorded during charge and discharge exhibit a doublet peak denoted by P1 and P2 respectively. They are generally assigned to electric quadrupolar transitions from 1s to 3d t_{2g} and 3d e_g orbitals. But assignment of the multiplet pre-edge peaks remains controversial and is beyond the scope of the present thesis. Research also proposed that they might be caused by electric dipole transition from 1s orbital to the p component in 3d-4p hybridized orbital. The d-p hybridization is formally forbidden for O_h symmetry but can be made possible through a Jahn-Teller deformation resulting in a noncentrosymmetric environment of the center atom. An intense pre-edge peak has been observed in K-edge XANES of Ti cation in a neptunite-type structure [35] and V cation in MgV_2O_6 and $Na_6V_{10}O_{28}$ [33] where the metal cations exhibit large deviation from the center of a regular octahedron. Thus, deformation of octahedral complexes could drastically enhance the intensity of pre-edge peak. [33]

Besides dependence on coordination number, pre-edge peak intensities are also closely correlated with the number of 3d electrons. They are found to be more intense where metal is at a higher oxidation state. As can be seen in Fig. 14, pre-edge peaks generally increase during charge and reach apex at point 5, then decrease monotonously during discharge with d orbitals gradually occupied. Possible explanation for T_d symmetrical complexes could be the higher extent of p component in p-d hybridized orbitals with decreasing number of d electrons which will enhance pre-edge peak intensities. Since electric dipole transitions to the 4p component accounts for most of the pre-edge peak intensity (much higher than the 1s-3d electric quadrupolar transitions), a higher degree of hybridization would result in bigger peak intensity. As in the case of complexes with a O_h symmetry like the battery material studied here, similar phenomenon can also be observed which confirmed the 4p-3d orbital mixing arising from structural deformation.

A more precise assignment of pre-edge peaks can be achieved by polarized x-ray absorption experiment. Since all orbitals are anisotropic except for s orbitals,

polarized XANES spectra could differentiate quadrupolar and dipolar transitions as well as clarify their contribution in the total pre-edge intensity. Penner-Hahn *et al.* investigated the rotation angle dependency of the pre-edge peak intensity for a square-planar $[CuCl_4]^{2-}$ which determined the component of the pre-edge peak as an electric quadrupolar transition to the d_{x2-y2} orbital [33]. The fact that pre-edge intensity was non-zero at any angle was proposed due to electric dipole transition which accounted for only one-forth of the total absorption.

Theoretical calculations could also serve as a useful tool in pre-edge evaluation. Since few compounds possess totally regular symmetry, the use of character table and group theory in interpretation of the pre-edge region is quite limited. They can be divided to two major categories: density function theory (DFT) calculations based on molecular orbital and FEFF program based on multiple scattering theories.

(1) Co pre-edge

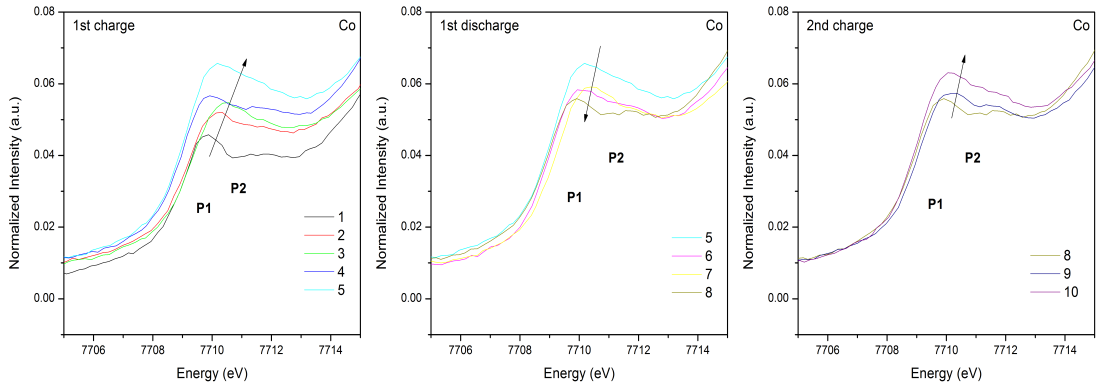

Fig. 18 Normalized XANES spectra of Co pre-edge during initial charge-discharge with two peaks denoted as P1 and P2. Arrows in the figures indicate the directions of the spectra shift.

Normalized XANES spectra of Co pre-edge during initial charge-discharge can be found in Fig. 18, which consists of two absorptions denoted as P1 and P2. The presence of two peaks indicates at least a partial high-spin configuration for Co^{3+}(d^6, $t_{2g}^4 e_g^2$). They are not well defined but distinguishable by Origin peak pre-analysis which indicates delocalized electrons in the band structure or an overlapping mixture (for Co^{3+}) of low-spin ($t_{2g}^6 e_g^0$), intermediate ($t_{2g}^5 e_g^1$) and high spin ($t_{2g}^4 e_g^2$). Co valent state in the beginning of the charge process has been discussed in the edge-step analysis. The energy separation of the two peaks is calculated to be 1.6 eV

on average, which is a slightly smaller value than the energy difference of Co t_{2g} and e_g orbitals (2.5 eV) found in O_h oxygen-coordinated complexes. [36] The variation of peak intensity and position agrees with above-mentioned theoretical analysis, but abnormality of a shift to smaller energy level during charging can be identified for Co sample 4. The same phenomenon is observed on sample 4 of Ni pre-edge spectrum. A chemical reduction at the oxide surface by the electrolyte has been proposed by Jiang *et al*. for Li-excess system. [23]

(2) Mn

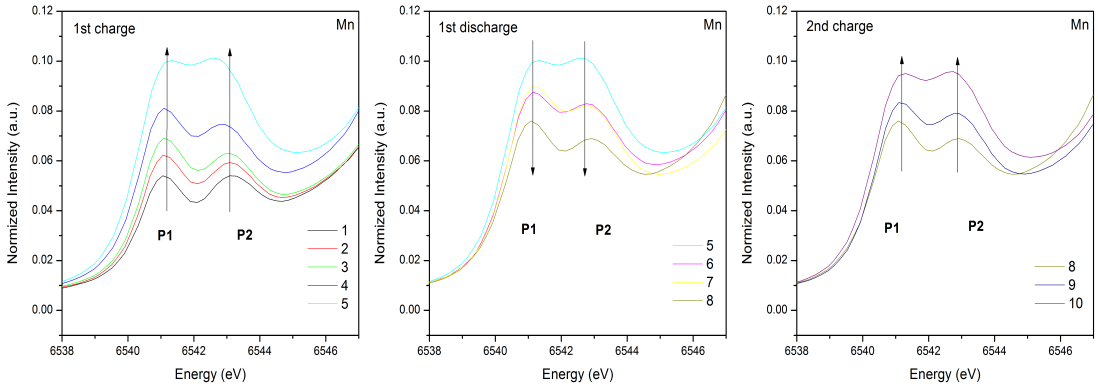

Fig. 19 Normalized XANES spectra of Mn pre-edge during initial charge-discharge with two peaks denoted as P1 and P2. Arrows in the figures indicate the directions of the spectra shift.

Two pre-edge peaks for Mn are more clearly discernible compared with those of Co and Ni. Peak positions remain unchanged with slightly bigger value for sample 5, which indicates the constant oxidation state of +4 for Mn during the whole process. It should be noted that the presence of two pre-edge peaks implies the Mn ions in their tetravalent state. The characteristic pre-edge feature of a single peak is observed for trivalent Mn compounds. [30]

(3) Ni

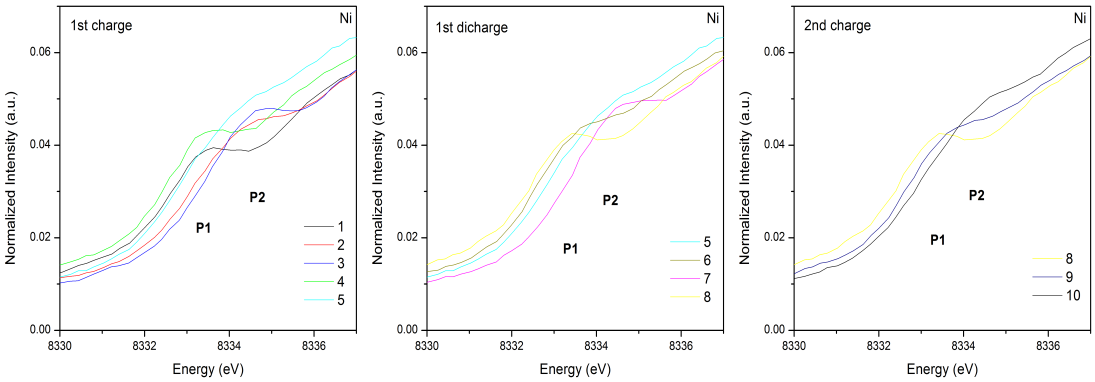

Fig. 20 Normalized XANES spectra of Ni pre-edge during initial charge-discharge with two peaks denoted as P1 and P2. Arrows in the figures indicate the directions of the spectra shift.

Ni gives the smallest pre-edge intensities among the three elements. Since for transition metals with an O_h structure, the intensity of pre-edge absorption increase as the site symmetry degenerates from a centrosymmetric to a non-centrosymmetric environment, the small absorption of Ni atom can be considered an evidence of relatively high symmetrical environment during different stages of charge and discharge. It is also evident from Fig. 20 that at initial state for Ni (+2 according to absorption edge analysis), two pre-edge peaks are still distinguishable. While the spin stage for Ni^{2+} (d^8, $t_{2g}^6 e_g^2$) allows only one transition 1s-e_g, it confirms the Jahn-Teller distortion in the samples in spite of the high symmetrical environment.

The detailed peak fitting results of pre-edge features during charge and discharge for Co, Mn and Ni can be found in Tab. 3.

Co	Peak 1		Peak 2	
	Position (eV)	Intensity (*100)	Position (eV)	Intensity (*100)
1	7709.6	2.17	7711.3	1.32
2	7709.9	2.14	7711.5	1.22
3	7710.1	1.98	7711.5	1.29
4	7709.7	2.80	7711.6	1.47
5	7709.8	2.00	7711.1	2.37
6	7709.7	2.41	7711.4	2.04
7	7710.0	2.06	7711.3	1.80
8	7709.6	1.77	7711.0	2.03
9	7709.7	2.40	7711.4	1.79
10	7709.7	2.16	7711.1	2.15

Mn	Peak 1		Peak 2	
	Position (eV)	Intensity (*100)	Position (eV)	Intensity (*100)
1	6541.0	3.27	6543.1	2.22
2	6543.1	3.91	6543.0	2.58
3	6541.1	4.48	6541.0	2.85
4	6543.0	5.13	6542.9	3.40
5	6541.1	5.18	6542.6	5.91
6	6541.0	1.67	6542.8	2.67
7	6541.0	5.72	6542.9	4.39
8	6542.9	4.81	6542.9	3.02
9	6540.9	5.22	6542.9	3.88
10	6542.6	5.20	6542.7	5.41

Ni	Peak 1		Peak 2	
	Position (eV)	Intensity (*100)	Position (eV)	Intensity (*100)
1	8333.4	1.12	8335.9	0.42
2	8334.2	1.28	8336.6	0.77
3	8334.5	1.78	8337.0	1.05
4	8333.3	1.55	8335.6	0.76
5	8334.0	1.45	8336.3	1.08
6	8333.5	1.50	8335.7	0.54
7	8334.4	1.57	8336.8	0.97
8	8333.3	1.54	8335.6	0.90
9	8333.6	1.40	8335.7	0.48
10	8334.2	1.30	8336.5	0.60

Tab. 3 Pre-edge peak position and intensity for the Co, Mn and Ni K-edge XANES during charge-discharge.

5.4 EXAFS Analysis

EXAFS spectra were analyzed to obtain a thorough understanding of the Co, Mn and Ni sites. The GNXAS package was used for treatment of EXAFS data based on Multiple Scattering (MS) theory. Its fundamental principle includes the decomposition of the EXAFS singles into a sum of several contributions, namely the irreducible n-body signals $\gamma^{(n)}$. This method also allows a direct least-square fitting of model theoretical function to raw experimental data where no data pre-process is necessary. In this section, a brief introduction of the GNXAS data processing process in the case of Ni K-edge will be presented. EXAFS analysis of the other two metals edges has been done following similar approaches.

5.4.1 GNXAS Processing

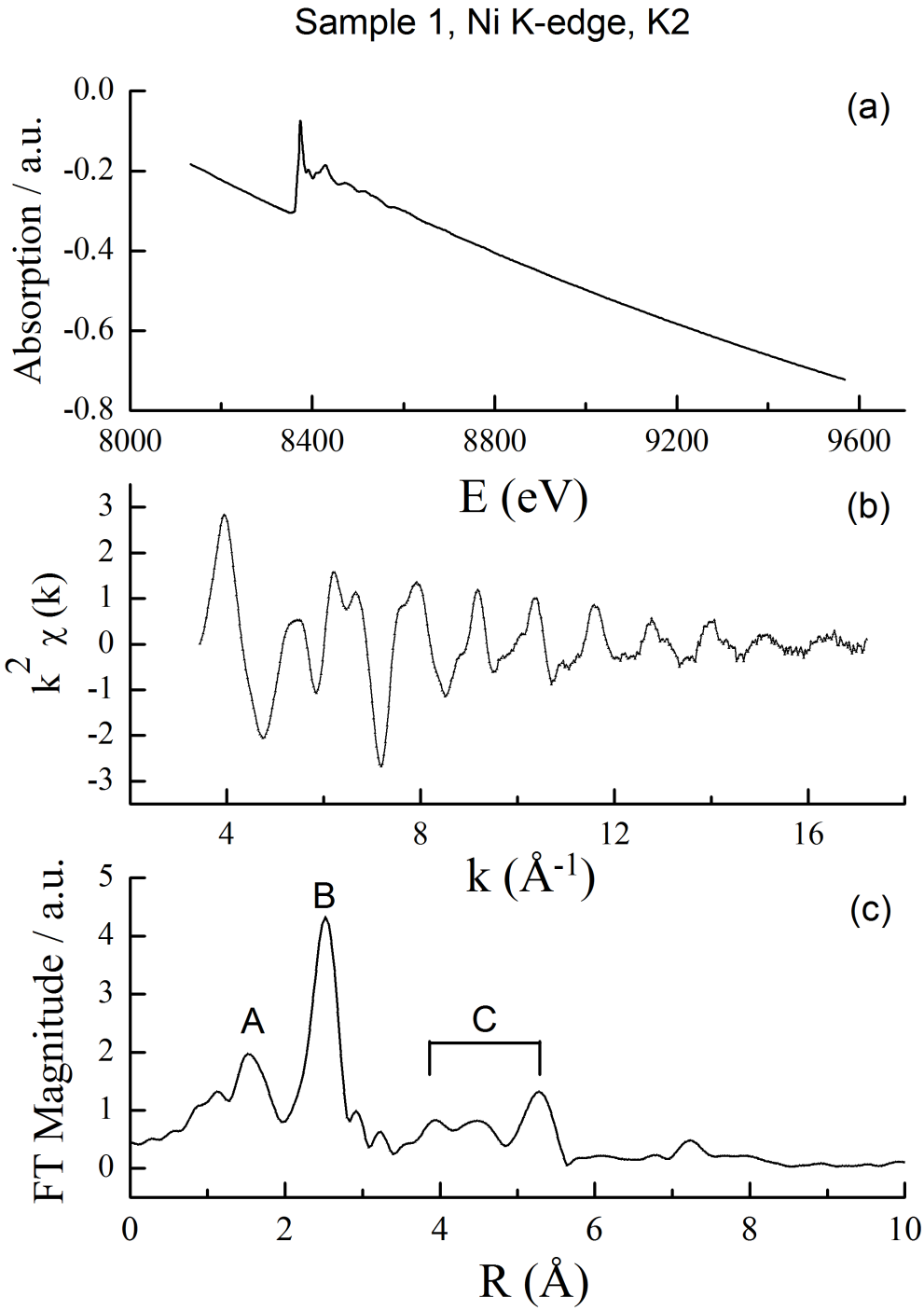

Fig. 21 Preliminary data subtraction of Ni K-edge EXAFS spectrum of sample 1. (a) Raw EXAFS experimental data; (b) k^2-extracted data; (c) Fourier Transform of the k^2-extracted data.

Output data of the Fitheo program of GNXAS package were exported and imported into Origin for EXAFS analysis. Both k-extracted and k^2-extracted treatments were conducted for a final comparison of the influence of k-range on the fitting results. The imported data include pa002.dat (absorption *vs*. Energy eV), pe002.dat (absorption in k-space), pt002.dat (multiple scattering contribution in k-space) and pf002.dat (Fourier Transform in R-space) from sample 1 to sample 10.

Fig. 21 (a) demonstrates a typical XAS absorption spectrum recorded at Ni K-edge before normalization. In this session, discussion will be focused on the EXAFS part ranging from around 8400eV and lasting up to the final point of the spectrum around 9600eV, which provides information about local atomic arrangement as well as structural disorder around the probed atomic site.

The normalized $\chi(k)$ function was then weighted with k^2 to account for the damping of oscillations with increasing k. The k^2-weighted extracted EXAFS signal can be found in Fig. 21 (b). The data appear structured and are of relatively high quality.

Fig. 21 (c) shows the magnitude of the data obtained by Fourier Transform of $k^2\chi(k)$ using a k-range of 3.6-17.2Å (k-range was set at 3.5-12.2Å for Co and 3.7-17.2Å for Mn, the low range of Co EXAFS can be attributed to the presence of Ni edge at 8.33keV). The FT spectra, which is a sort of radial structure function around the metal site, is composed of information of several peaks. Peak A can be related to Ni-O correlation of the first shell and peak B indicating Ni-Ni/M (M: transition metal) correlation of the second shell. Peak C may refer to numerous multiple scattering Ni-M and Ni-O interaction of the outershells.

(1) Structural Model (Program Crymol and Gnpeak)

As a custom in any EXAFS fitting procedure, the experimental signal is compared to the theoretical one, which is calculated from an initial structural model. An input command containing the relevant structural information and input parameters was prepared from cif file obtained from research work on the crystal structure of $Li[Ni_{1/3}Co_{1/3}Mn_{1/3}]O_2$ by Zhu *et al*.[37] The structure code program that produces the appropriate format for the single theoretical calculation is called Crymol.

A representative input card for Crymol can be found in Fig. 22:

```
SYM
LiNiO2 ! Lin et al, Cryst. Growth Design 2012,12,1232
H ! Hexagonal
2.8150,14.0516   !a,c
4                  !n atomi
    1     'Li'      0.0000    0.0000    0.0000     6    0.    1.1
    2     'Ni'      0.0000    0.0000    0.5000     6    0.    1.1
    3     ' O'      0.0000    0.0000    0.2397     6    0.    1.1
    4     ' O'      0.0000    0.0000   -0.2397     6    0.    1.1
3
0.,0.,0.
0.3333,0.6666,0.6666
0.6666,0.3333,0.3333
1
1,' x   ','   y  ','      z',0.,0.,0.
N,Y,N
3
'Ni'  ' O'   2.5
'Ni'  'Ni'   3.8
'Ni'  ' O'   2.5
6.5
Ni1
1,2               ! TOTAL N. AND NUMBERS of the photoabsorber
.1                ! tolleranza phase shifts
1                 ! 1=K-edge,2=L1-edge .....
1                 ! Pot. calc. using 0-given radii 1-Norman crit.
502.,0.           ! Core Ionization Potential,EF
3,-.5,75.,.050     ! IMESH,EMIN,EMAX,DE calcolo fasi
5,-1.             ! Tipo calcolo, gamma
'S',1,40.,20.,'S',' ','S'
```

Fig. 22 Representative input card of model structure of $LiNiO_2$. Corresponding unit cell type (line 3), unit cell dimensions (line 4), atomic positions (line 5-9), translational and rotational symmetry operation (line 10-15), maximum neighbor distance (line 17-20) and cut off distance (line 21) are presented with their proper format.

Furthermore, thanks to the signal calculation program Gnpeak, the major two, three, and four-body local configurations around the photoabsorber atom are identified and analyzed based on an initial structural model from Crymol output. They are often referred to as “peaks” of the two-body (g_2), three-body (g_3) and four-body (g_4) distributions in cluster. The two-body terms contain specification of the distance and of the two atomic types. The three-body terms are associated with two shortest bond lengths, the angle in between as well as three atomic types. The four-body terms are associated with four atoms, three bond lengths and the angles between them. A scheme of the n-body distribution can be seen in the figure below:

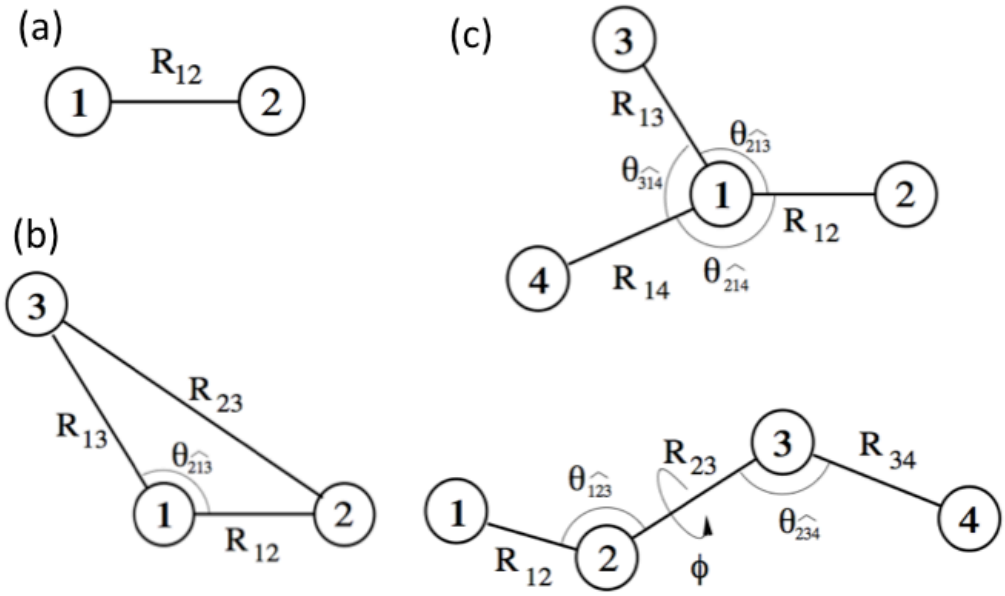

Fig. 23 Scheme of two-body, three-body, and four-body configuration. [38]

Each of the configurations would generate several single and multiple scattering contributions for the theoretical calculation of the model EXAFS signals, which is then fit to the non-Fourier-filtered experimental data. In the case of Ni samples, a number of g_2 and g_3 peaks are found. Output file of Gnpeak containing relevant two-body and three-body are exported from Ni1.gnp and saved as graph, as shown in Fig. 24 and Fig. 25.

```
*****************************************************
*** PEAKS OF THE TWO-BODY DISTRIBUTION IN CLUSTER ***
*****************************************************

CENTRAL ATOM      1 TYPE     Ni

  PEAK     DISTANCE      # ATOMS        TYPES
    1       1.92225       6.00000       Ni     0
    2       2.81500       6.00000       Ni    Ni
    3       2.85043       6.00000       Ni    Li
    4       3.40870       6.00000       Ni     0
    5       3.65763       2.00000       Ni     0
    6       4.00614       6.00000       Ni    Li
    7       4.42080      12.00000       Ni     0
    8       4.61546      12.00000       Ni     0
    9       4.89626      12.00000       Ni    Li
   10       4.91688      12.00000       Ni    Ni
   11       5.66572      12.00000       Ni    Ni
   12       5.94496      18.00000       Ni     0
```

Fig. 24 Peaks of the two-body distribution in cluster calculated from input structural model (12 peaks obtained in total).

```
*******************************************************
*** PEAKS OF THE THREE-BODY DISTRIBUTION IN CLUSTER ***
*******************************************************


  PEAK        COORDINATES      CONF.#  PhP     ATOM TYPES     ATOM #      FREQ.
 1/  1   1.9219 1.9226  85.86    6.00    1     Ni     0     0    1  2 11    3.2314
 2/  2   1.9221 1.9223  94.15    4.00    3      0    Ni    Ni    2  7  1    3.3297
      --->    long bond coincides with peak    2 of the g2
 3/  3   1.9222 1.9223  94.14    6.00    1     Ni     0     0    1  4  2    3.3298
 4/  4   1.9222 1.9223  94.14    8.00    2      0    Ni    Ni    2  1  5    3.3298
      --->    long bond coincides with peak    2 of the g2
 5/  5   1.9223 2.0907  90.42   12.00    2      0    Ni    Li    2  1 14    3.4317
      --->    long bond coincides with peak    3 of the g2
 6/  6   1.9219 1.9226 179.96    3.00    1     Ni     0     0    1  2  6    3.8445
 7/  7   1.9223 2.6184  96.09    6.00    2      0    Ni     0    2  1 32    3.9747
```

Fig. 25 First 7 peaks of the three-body distribution in cluster calculated from input structural model (102 peaks obtained in total).

(2) Multiple Scattering Calculation and MS signal evaluation (Program Gnxas)

The acronym of program Gnxas is composed of GN and XAS, which implies a combination of n-body distribution functions and X-ray Absorption Spectroscopy. [38] In this step, signals associated with 2, 3 and 4 atoms clusters representing reference configurations in the two-body g_2, three-body g_3 and four-body g_4 multiple scattering terms are calculated in an *ab initio* approach and denominated $\gamma^{(n)}$ (n denotes the n-body distribution).

The first 11 g_2 configurations and 8 g_3 configurations were selected in input file for further fitting analysis. The contributions from the three-body terms are later found to be negligible thus they are not included in the Fitheo input file. A relative large number of n-body contributions were chosen in this step for the purpose of signal checking and comparison. It also makes it easier in the fitting procedure where only small modifications have to be made in the input file of the fitting procedure to include more or less scattering signals. In all cases the Li contribution to EXAFS was ignored on account of the low back scattering ability of lithium.

The output file Ni1GNPLO was plotted directly and the graphs were extracted by the “screenshot” function of the Linux system. They contribution of each signal is shown in

Fig. 26.

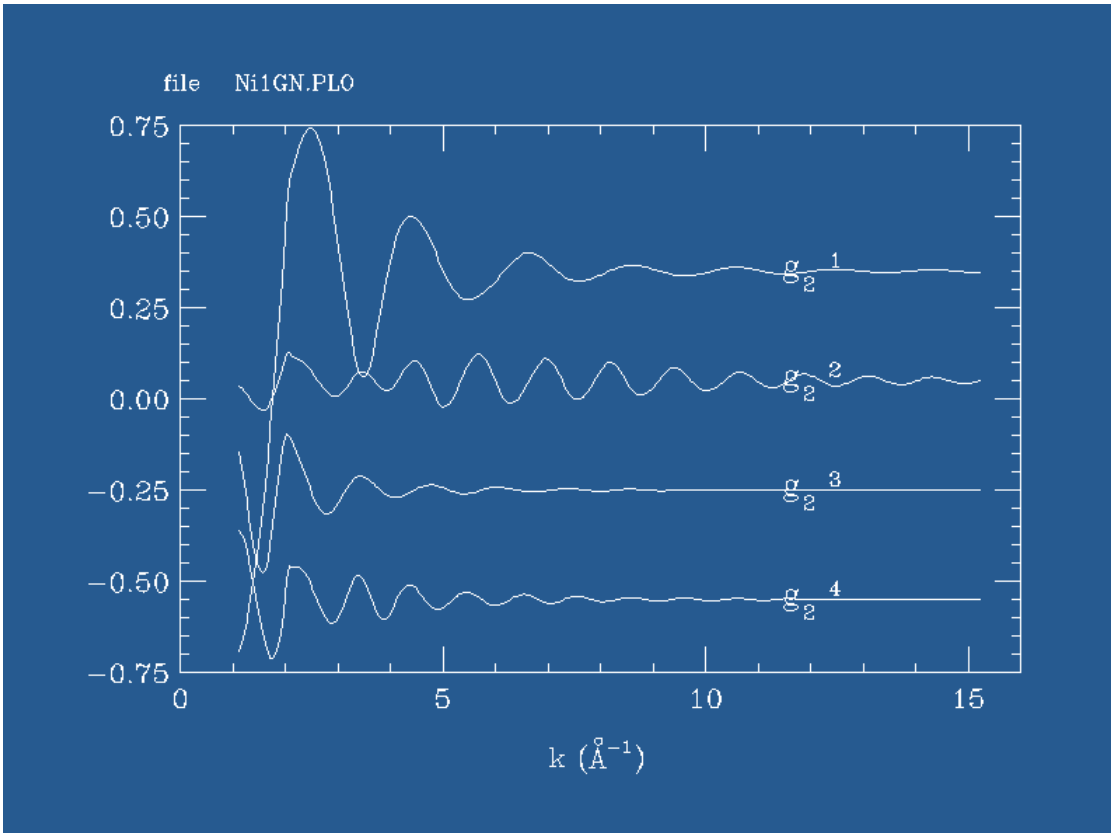
file Ni1GN.PLO
0.75
0.50
0.25
0.00
−0.25
−0.50
−0.75
0
5
10
15
k (Å^{-1})
g_2 1
g_2 2
g_2 3
g_2 4

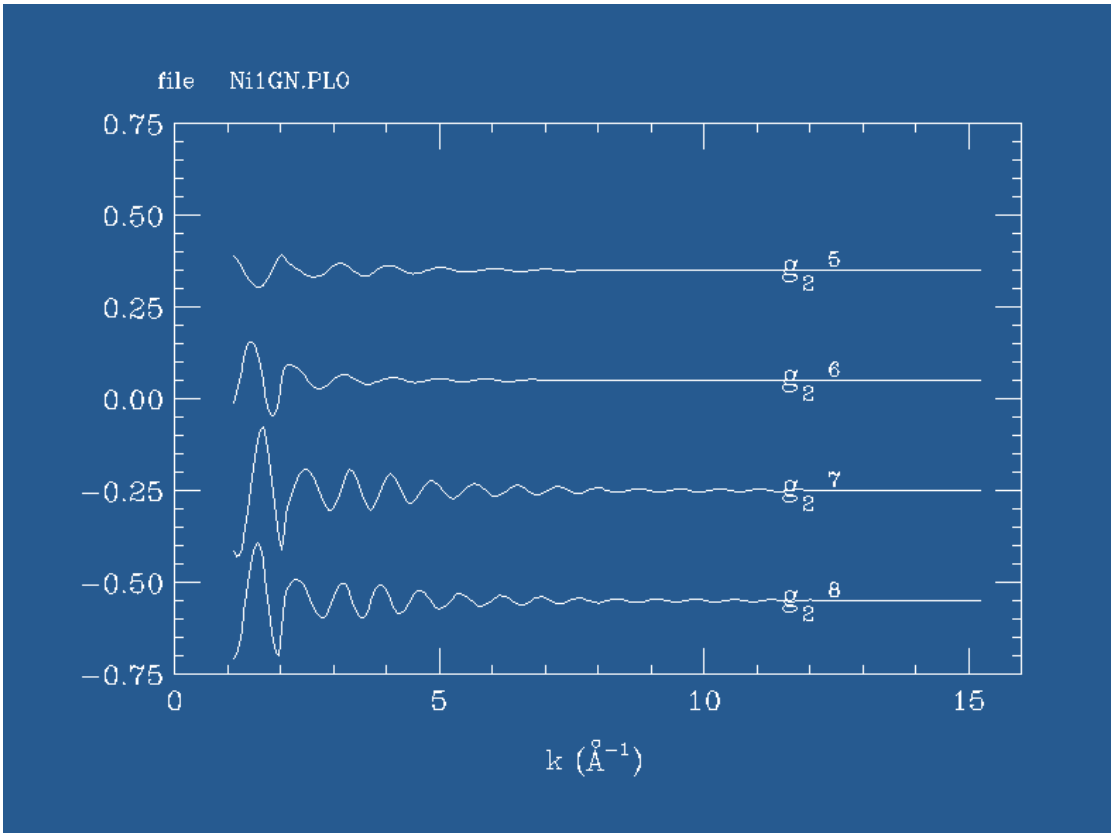
file Ni1GN.PLO
0.75
0.50
0.25
0.00
−0.25
−0.50
−0.75
0
5
10
15
k (Å^{-1})
g_2 5
g_2 6
g_2 7
g_2 8

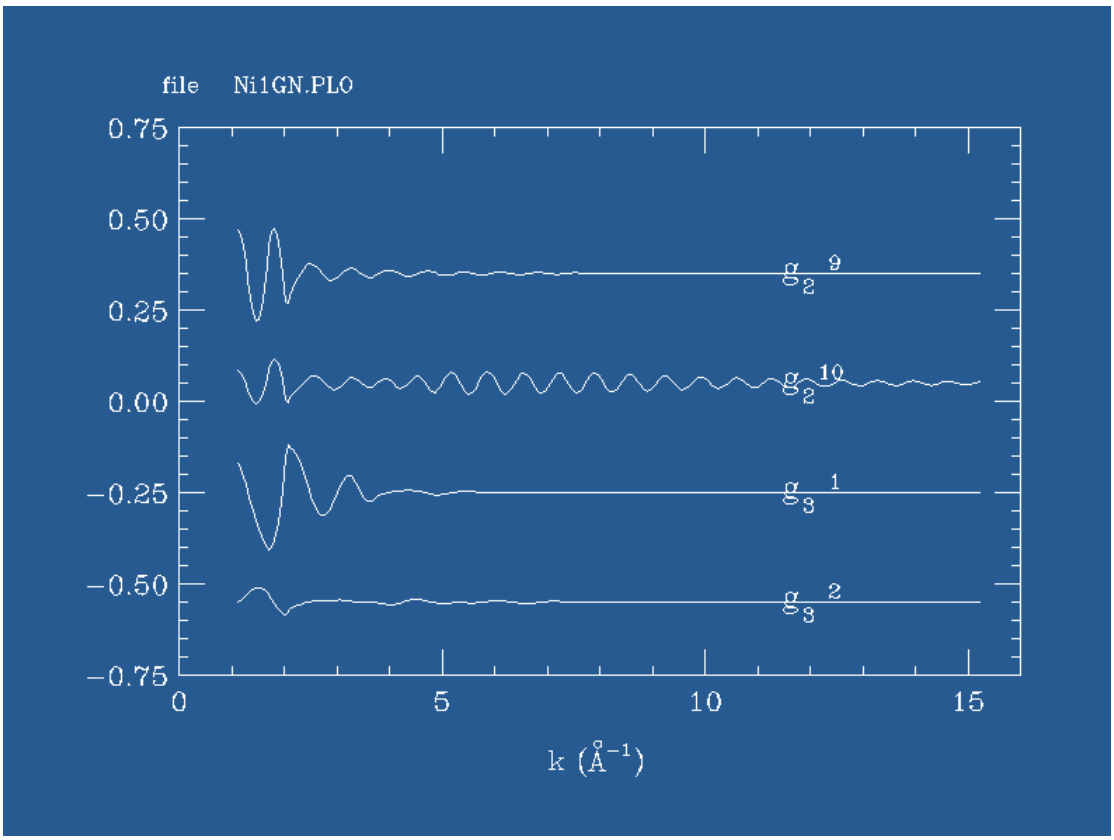
file Ni1GN.PLO
0.75
0.50
0.25
0.00
−0.25
−0.50
−0.75
0
5
10
15
k (Å^{-1})
g_2^9
g_2^{10}
g_3^1
g_3^2

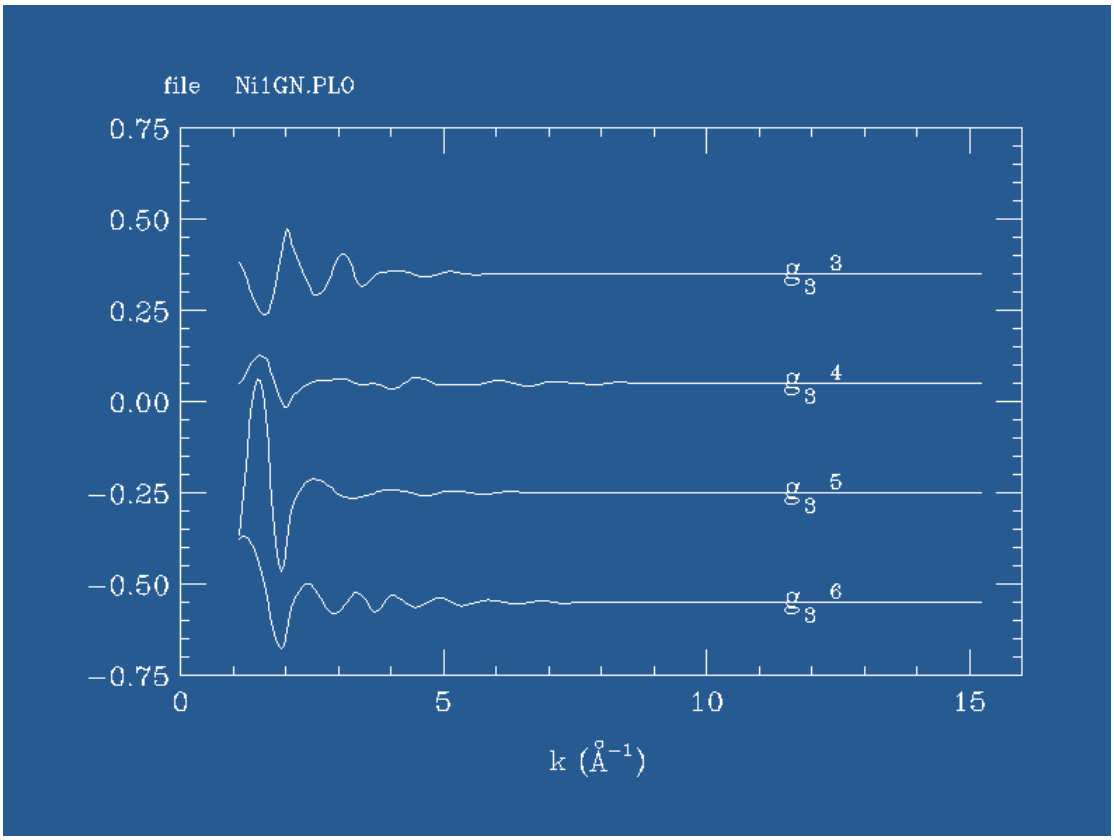
file Ni1GN.PLO
0.75
0.50
0.25
0.00
−0.25
−0.50
−0.75
0
5
10
15
k (Å^{-1})
g_3^3
g_3^4
g_3^5
g_3^6

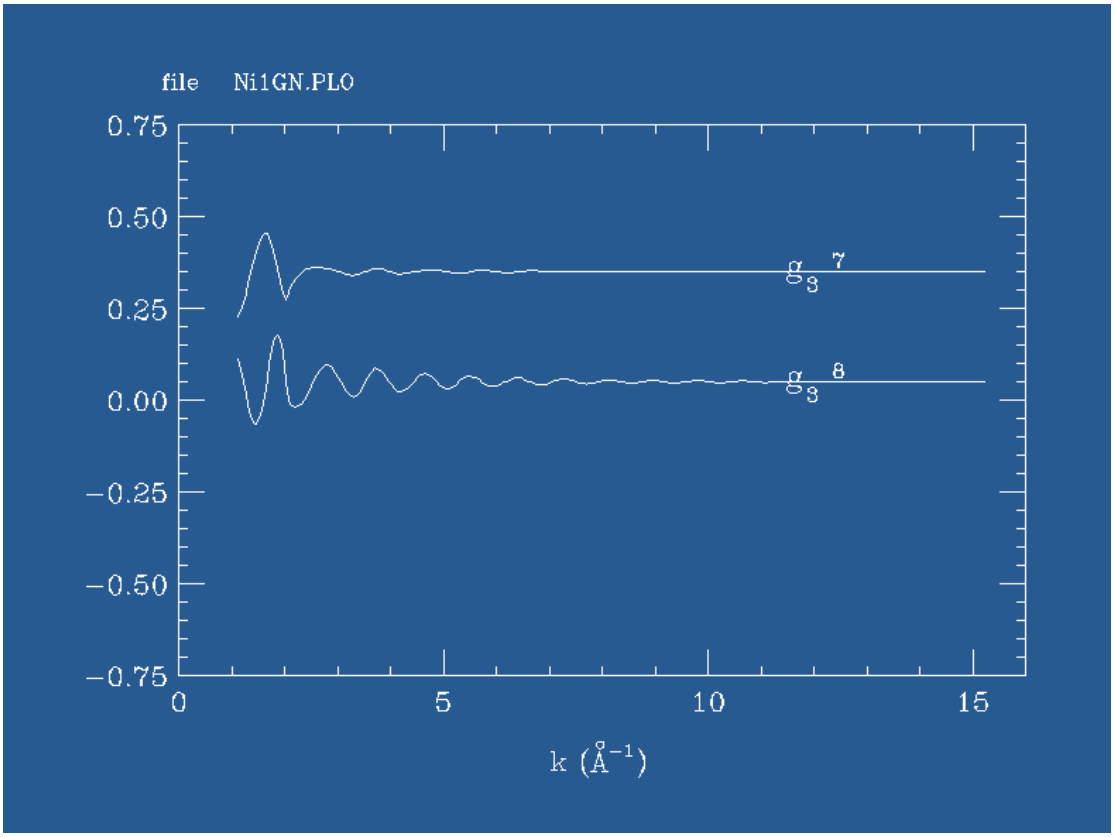
file Ni1GN.PLO
0.75
0.50
0.25
0.00
−0.25
−0.50
−0.75
0
5
10
15
k (Å^{-1})
g_3^7
g_3^8

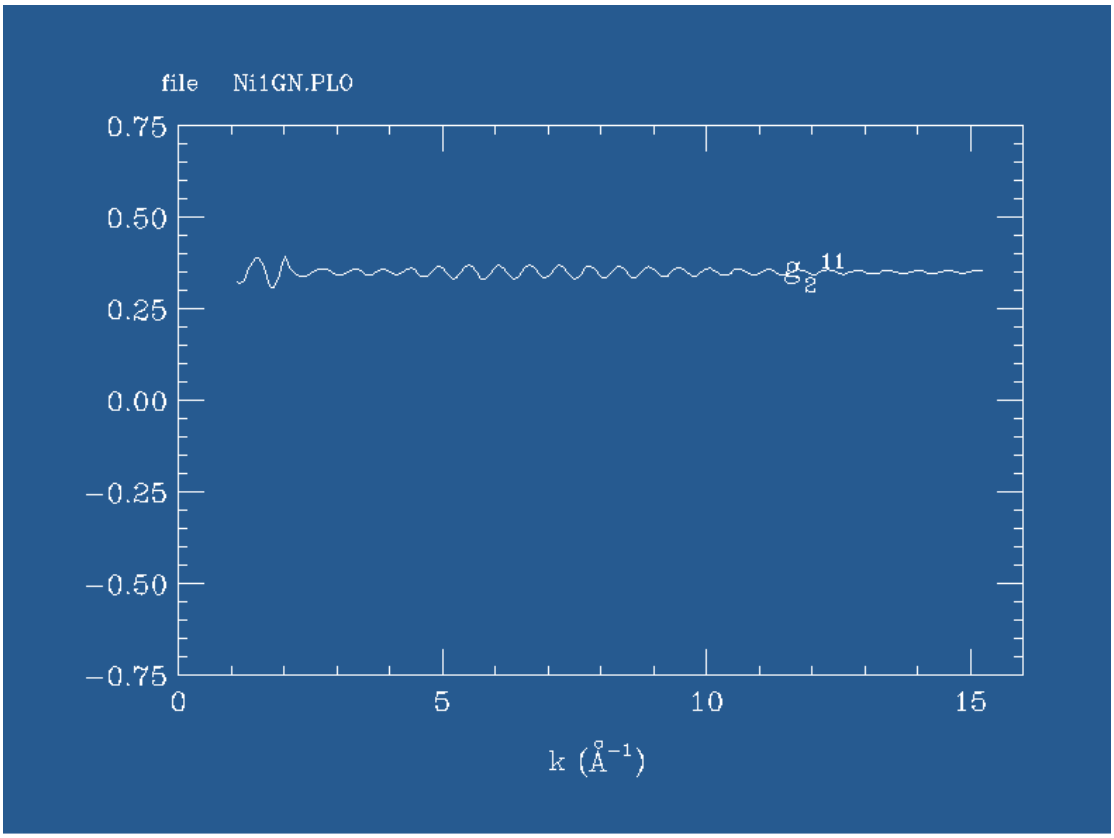
file Ni1GN.PLO
0.75
0.50
0.25
0.00
−0.25
−0.50
−0.75
0
5
10
15
k (Å^{-1})
g_2^{11}

Fig. 26 Contributions for the total theoretical signal associated with each input n-body distributions for Ni. $11\gamma^{(2)}$ signal and $8\gamma^{(3)}$ signals are selected. Note that in the figure g_n is used for each irreducible n-body signal (*e.g.* $g_2^{\ 1}$ indicates the first one of two-body contributions) while in the present thesis $\gamma^{(n)}$ are used with $\gamma_1^{(2)}$ meaning the first one of two-body contribution.

Each signal can be further evaluated in terms of the relevant intensity. The higher the intensity, the higher the relevance, and therefore the more important role it plays in the final fitting procedure. In the process of evaluating these signals, the intensities of k before 3-4Å should not be considered since they are out of the range of successive EXAFS fitting. As exhibited in the Fig. 26, the most intense signals are $\gamma_1^{(2)}$ and$\gamma_2^{(2)}$, which are related to the Ni-O first shell and Ni-Ni second shell. Both signals have degeneracy of 6 (hence the coordination number CN=6). In addition, $\gamma_3^{(2)}$, $\gamma_6^{(2)}$ as well as $\gamma_9^{(2)}$ appear to be the least contributing one. This is expected because they correspond to scattering of the lightest element: Li. On the other hand, signals related to Ni-Ni/M interactions, for example, should be included in the fitting process.
Fig. 26 also suggests that signals of three-body peaks could be overlooked.

(3) Fitting (Program Fitheo)

Fitting process is performed by Fitheo program which builds a model absorption signal composed of structural oscillation $\chi(k)$ and compares it with the experimental absorption signal, in the premise that all single and multiple scattering contributions have been calculated *ab initio* for a chosen cluster of atoms. The inclusion of different number of two-body scattering paths, namely $4\gamma^{(2)}$, $5\gamma^{(2)}$ and $6\gamma^{(2)}$ were tried out and the residuals of fitting spectrum were visually inspected. Combing the analysis in the previous session about MS evaluation, five two-atom contributions were included: $\gamma_1^{(2)}$ with degeneracy of 6; $\gamma_2^{(2)}$ with degeneracy of 6; $\gamma_4^{(2)}$ with degeneracy of 6; $\gamma_{10}^{(2)}$ with degeneracy of 12; An Fitheo input file constructed from the selected n-atom multiple scattering paths was prepared for each sample during charge-discharge, allowing modification of bond distance and Debye-Waller factor. S_0^2 for Mn, Co and Ni were fixed to be 0.72, 0.88 and 0.85 respectively, according to literature.

A typical fitting outcome includes both output files and graphs. The output file presents the relevant structural parameters (bond distances and EXAFS Debye-Waller factor) together with the non-structural terms (E_0 values, S_0^2 and the final value of the residual function R). Fig. 27 reports a typical Fitheo output for

EXAFS analysis at the Ni K-edge, obtained from sample 1.

```
 DATE: 30/ 5/2013
  EDGE=   8370.
  Edge energy selected by user
  JUMP=   0.130547076
  Spline mode (user preferences): NFIT1= 3
  Spline coefficients:
  5.58010796
 -57.9526843
  166.827734
 -2.91275009
 -47.2401993
 -178.115703
  0.0521804
  0.35203217
  0.789266853
  FILE: ./../../../measurement/1_Ni_000.txt
  FIT:  449 points, 12 parameters,  5 g2,  0 g3,  0 g4
  Energy range   8415.0  9500.0   weight ** 2.0
            R value = .22712E-05
  St. Dev. of exp. data (aut. determined) =.17430E-03
  Normalized St. Dev. of exp. data =.13351E-02 edge n.1
  Expected R value for given weight and St. Dev.=.94845E-06
  Suggested ERROR DEF (95%) for  12 free parameters  ->>>.44415E-07<<<
      X( 2)=      1.0000000
      X( 3)=      2.0000000
      X( 6)=   8363.8616577
      X(13)=      1.5001484
      X(15)=      1.9972748
      X(16)=      0.0050869
      X(17)=      2.8609019
      X(18)=      0.0057991
      X(19)=      3.3920272
      X(20)=      0.0104662
      X(21)=      5.0350865
      X(22)=      0.0106316
      X(23)=      5.9118921
      X(24)=      0.0084315
      X(53)=      0.8500000
```

Fig. 27 Typical Fitheo output file for Ni (five single scattering selected).

A detailed graphic output is also produced for in-time visual checkout of the fitting process. Important files include:

paNi.dat: experimental absorption data, background modeling and near edge structures indicating the edge position.

peNi.dat: theoretical $\chi(k)$, experimental $\chi(k)$ as well as the residual in the k-space ($Å^{-1}$).

ptNi.dat: all n-body contributions included in the fitting process, their sum theoretical $\chi(k)$, experimental $\chi(k)$ as well as the residual in the k-space ($Å^{-1}$).

pfNi.dat: Fourier Transform of theoretical $\chi(k)$, experimental $\chi(k)$ as well as of the

residual in the R-space (Å).

Original data of paNi.dat, peNi.dat, ptNi.dat and pfNi.dat (k-weighted and k^2-weighted respectively) were exported to Origin for a better visual presentation of the output graphs.

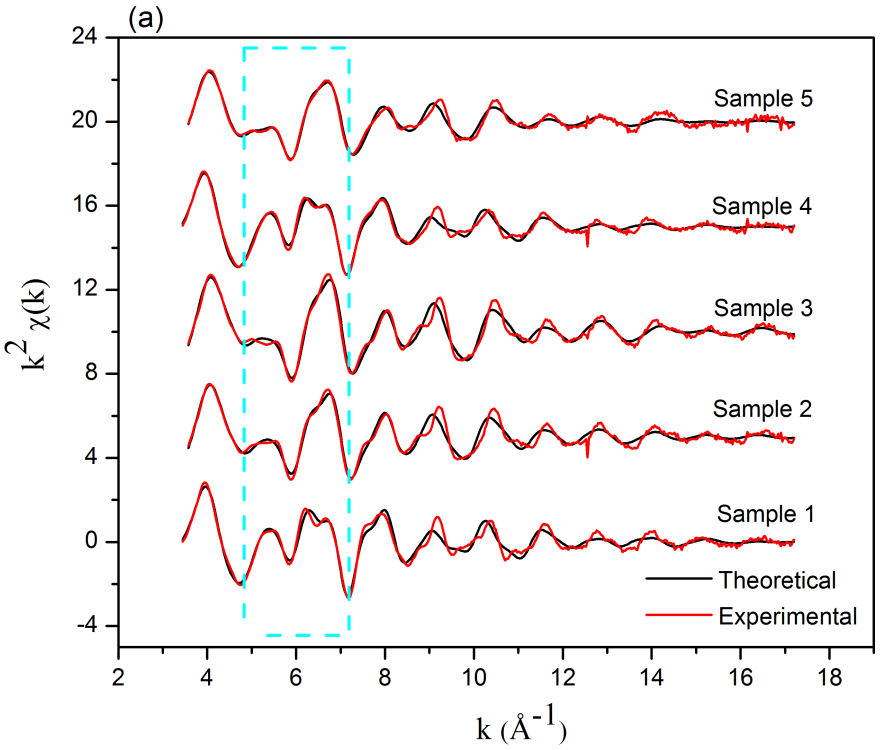

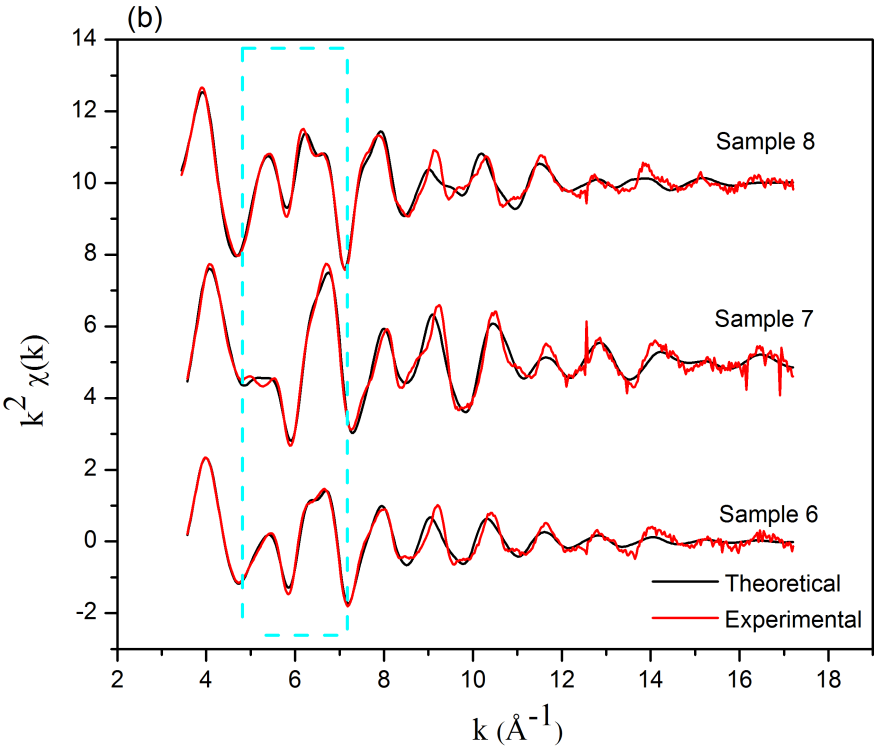
(b)
Sample 8
Sample 7
Sample 6
Theoretical
Experimental
k² χ(k)
k (Å⁻¹)

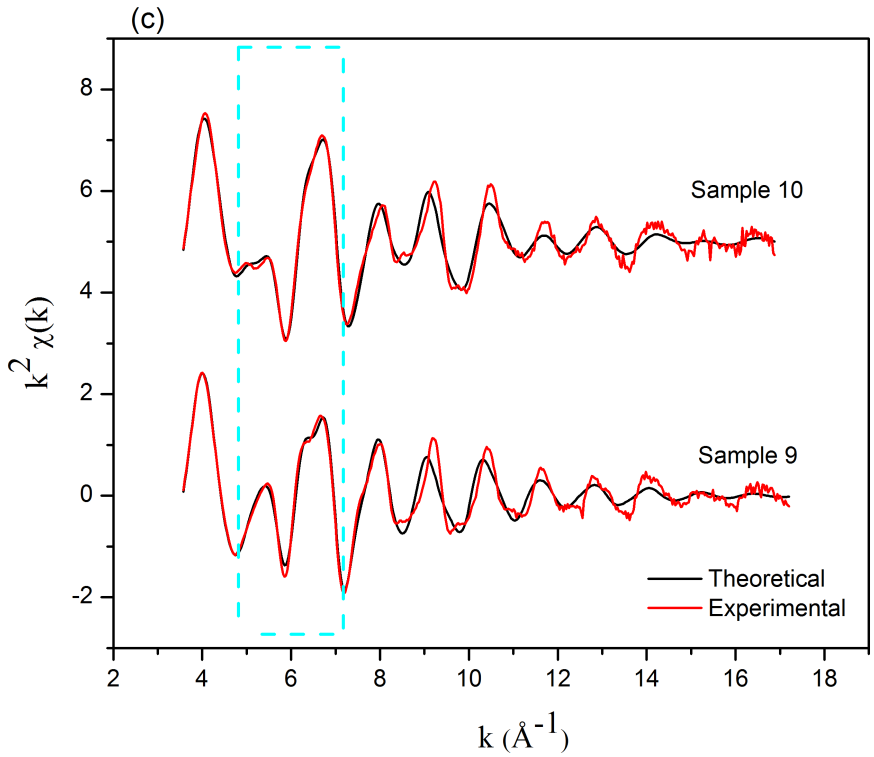
(c)
Sample 10
Sample 9
Theoretical
Experimental
k² χ(k)
k (Å⁻¹)

Fig. 28 Comparison of the total theoretical signal with experimental one for Ni K-edge (k^2-weighted) (a) sample 1-5 during initial charge; (b) sample 6-8 during initial discharge and (c) sample 9-10 during second charge.

It is worth mentioning that the weight of both k and k^2 were applied in the Fitheo minimization process. But k^2 weight was finally used for following EXAFS analysis of each element. This is because original experimental data are already of high quality so the use of higher k weight will not drastically magnify the noises. Since the high-k oscillations are also of importance in the present project, a bigger k-weighting could also serve to emphasize the higher portions of the measured $\chi(k)$ spectrum.

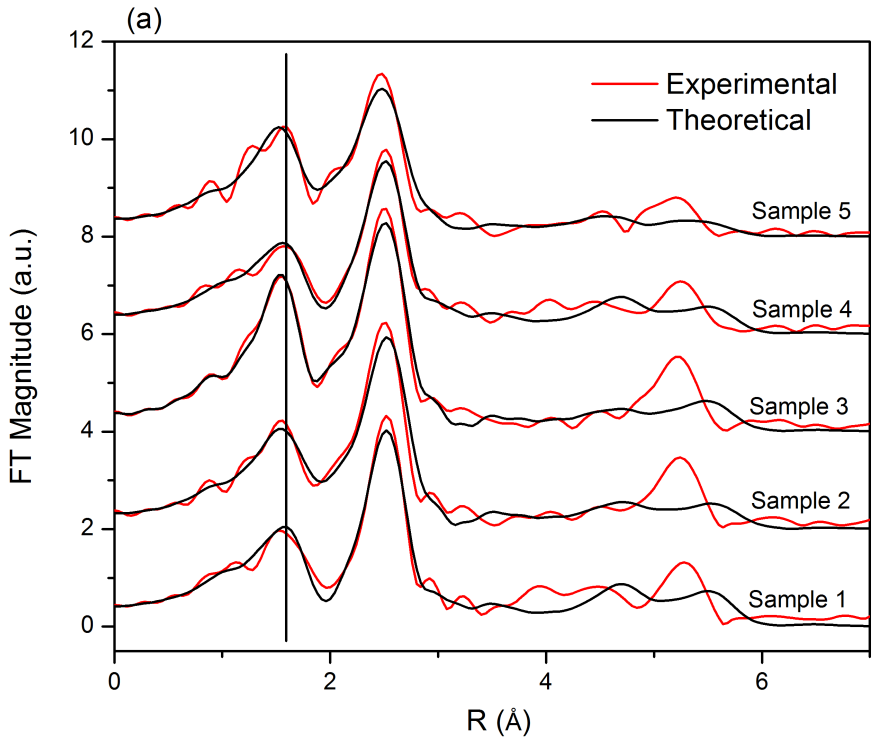

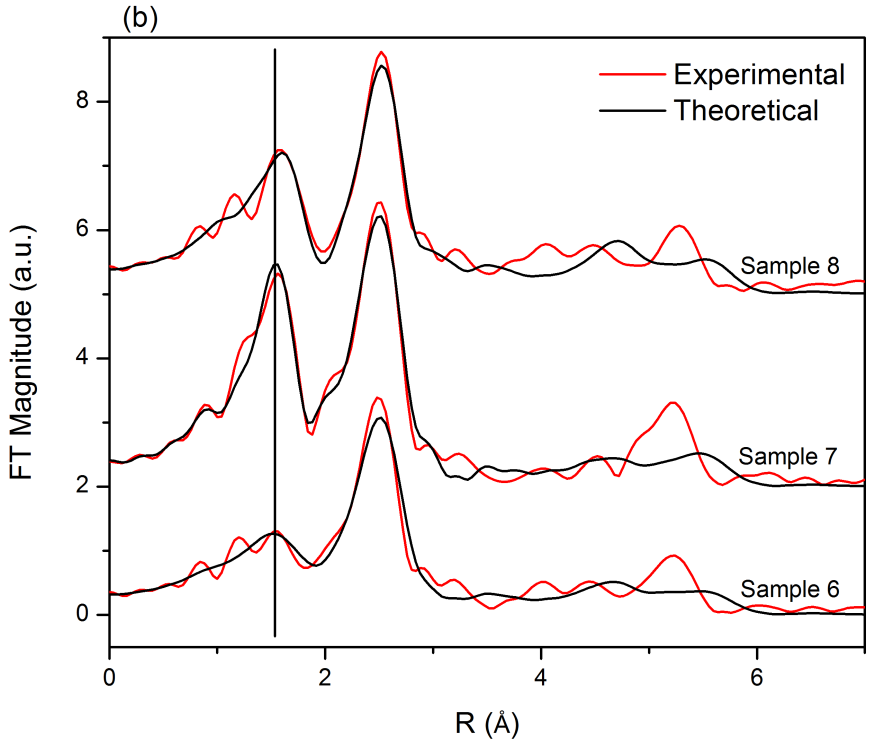
(b)
Experimental
Theoretical
Sample 8
Sample 7
Sample 6
FT Magnitude (a.u.)
R (Å)
0
2
4
6
8

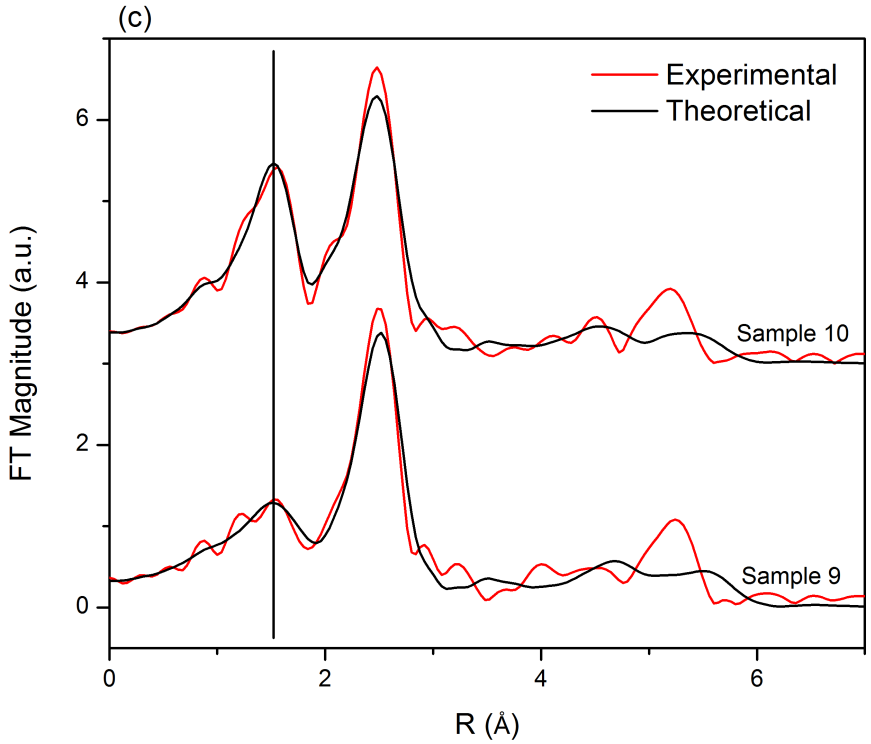
(c)
Experimental
Theoretical
Sample 10
Sample 9
FT Magnitude (a.u.)
R (Å)
0
2
4
6

Fig. 29 Comparison of the total theoretical FT with experimental one for Ni K-edge (k^2-weighted) (a) sample 1-5 during initial charge; (b) sample 6-8 during initial discharge and (c) sample 9-10 during second charge (not corrected for phase shift).

Fig. 28 displays the comparison of the k^2-extracted EXAFS signals of the investigated samples in red and theoretical curves in black whereas the corresponding Fourier Transform (FT) are reported in
Fig. 29. Both figures are actually composed of three panels, which correspond to the first charge (a), first discharge (b), and second charge (c).

From all graphs, we can observe that the theoretical curves match well with the experimental ones, indicating the reliability of the selected structural model and the accuracy of the data analysis. Peak intensity and broadness of the radial structure function in
Fig. 28 correlate to the coordination number (CN) and Debye-Waller factors (σ), which reflect the thermal fluctuations and local order. [30] During the first charge, the sinusoidal curves around 5-7 $Å^{-1}$ on
Fig. 28 (a) appear having the most variable features, most likely due to a first-shell shortening which exert certain influence on the scattered waves. The composition of the corresponding FT curve of
Fig. 29 confirms this hypothesis, seen in the shift of the first peak to lower R value.

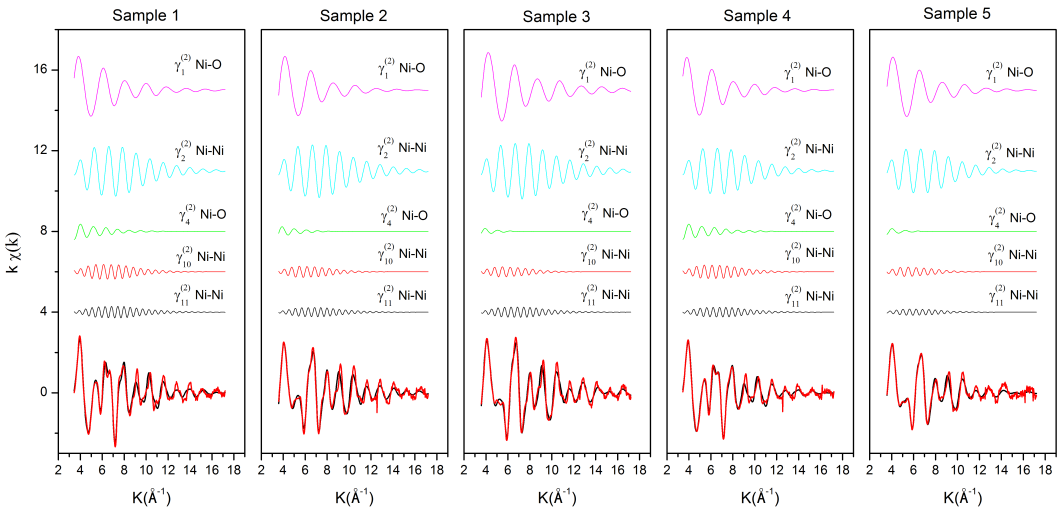

Fig. 30 Details of the EXAFS analysis of sample 1-5 of Ni K-edge. The sample number is indicated at the top of each panel. The figure shows the individual EXAFS

signal, in terms of two-body contributions. At the bottom, the comparisons of the total theoretical signal (black line) with experimental (red line) are also presented.

Fig. 30 reports the details of the EXAFS analysis (best fits) of sample 1-5 at Ni K-edge. The contributions of each two-body signal to the total theoretical one, as well as comparisons of the theoretical signal with experimental one are presented. Even though the first two signals, due to the Ni-O and Ni-M interactions are the most intense one, this confirms the choice of the most relevant MS contributions to be included in the fitting calculation described above. All the signals are rather important in determining the total theoretical signal.

The structural parameters obtained by fitting for Mn/Ni/Co was summarized in Tab. 4, Tab. 5 and Tab. 6.

Mn	**Mn-O**		**Mn-Mn**		**Mn-O**		**Mn-Mn**	
	R (Å)	**σ^2 (Å^2)**	**R (Å)**	**σ^2 (Å^2)**	**R (Å)**	**σ^2 (Å^2)**	**R (Å)**	**σ^2 (Å^2)**
1	1.881	0.0012	2.873	0.0025	3.600	0.0068	5.022	0.0054
2	1.877	0.0018	2.862	0.0026	3.600	0.0100	5.024	0.0103
3	1.874	0.0023	2.859	0.0029	3.600	0.0117	5.025	0.0126
4	1.872	0.0039	2.877	0.0016	3.592	0.0193	5.026	0.0108
5	1.864	0.0042	2.859	0.0021	3.560	0.0257	4.986	0.0121
6	1.867	0.0039	2.868	0.0018	3.566	0.0227	5.007	0.0116
7	1.867	0.0035	2.858	0.0031	3.600	0.0170	5.009	0.0136
8	1.874	0.0039	2.885	0.0019	3.599	0.0170	5.032	0.0101
9	1.870	0.0037	2.869	0.0017	3.584	0.0199	5.020	0.0118
10	1.863	0.0041	2.858	0.0020	3.550	0.0262	4.986	0.0117

Tab. 4 Results of structural analysis of Mn.

Ni	Ni-O		Ni-Ni		Ni-O		Ni-Ni		Ni-Ni	
	R (Å)	σ^2 (Å^2)	R (Å)	σ^2 (Å^2)	R (Å)	σ^2 (Å^2)	R (Å)	σ^2 (Å^2)	R (Å)	σ^2 (Å^2)
1	2.000(4)	0.0051(5)	2.863(4)	0.0057(5)	3.40(2)	0.011(3)	5.04(2)	0.011(2)	5.92(2)	0.009(2)
2	1.911(5)	0.0065(6)	2.854(6)	0.0053(4)	3.52(4)	0.02(1)	5.03(2)	0.014(3)	5.93(2)	0.010(2)
3	1.885(3)	0.0034(4)	2.841(4)	0.0048(4)	3.48(6)	0.03(1)	4.99(2)	0.016(3)	5.90(2)	0.009(2)
4	1.997(5)	0.0057(5)	2.859(6)	0.0066(5)	3.39(2)	0.010(5)	5.03(1)	0.012(2)	5.94(2)	0.010(5)
5	1.888(3)	0.0057(4)	2.830(4)	0.0071(3)	3.31(6)	0.03(1)	4.93(2)	0.017(2)	5.90(2)	0.015(3)
6	1.947(4)	0.0092(5)	2.854(3)	0.0070(4)	3.42(4)	0.018(4)	5.01(2)	0.015(2)	5.94(2)	0.012(2)
7	1.885(3)	0.0030(5)	2.838(3)	0.0050(5)	3.48(7)	0.03(1)	4.97(2)	0.017(3)	5.91(2)	0.011(3)
8	2.014(3)	0.0045(5)	2.870(4)	0.0066(4)	3.40(2)	0.009(3)	5.05(2)	0.011(2)	5.95(2)	0.010(2)
9	1.946(3)	0.0092(6)	2.853(3)	0.0065(4)	3.44(3)	0.02(2)	5.02(2)	0.014(3)	5.94(2)	0.012(3)
10	1.885(5)	0.0051(4)	2.829(3)	0.0066(4)	3.31(7)	0.03(1)	4.93(2)	0.017(2)	5.90(2)	0.013(2)

Tab. 5 Results of structural analysis of Ni. Errors are indicated in parenthesis for Ni sample 1-5. They were calculated by CONTOUR plots among the highest correlated variables.

Co	Co-O		Co-Co		Co-O		Co-Co	
	R (Å)	σ^2 (Å^2)	R (Å)	σ^2 (Å^2)	R (Å)	σ^2 (Å^2)	R (Å)	σ^2 (Å^2)
1	1.902	0.0010	2.842	0.0058	3.551	0.0072	5.009	0.0096
2	1.884	0.0010	2.832	0.0056	3.542	0.0103	4.994	0.0136
3	1.875	0.0010	2.827	0.0053	3.515	0.0116	4.977	0.0157
4	1.889	0.0010	2.839	0.0044	3.459	0.0250	4.989	0.0120
5	1.874	0.0010	2.827	0.0052	3.496	0.0257	4.946	0.0142
6	1.882	0.0010	2.830	0.0051	3.419	0.0294	4.965	0.0136
7	1.874	0.0010	2.828	0.0056	3.523	0.0170	4.963	0.8800
8	1.894	0.0010	2.844	0.0046	3.444	0.0246	4.994	0.0111
9	1.886	0.0010	2.833	0.0051	3.522	0.0210	4.984	0.0148
10	1.873	0.0010	2.822	0.0049	3.456	0.0216	4.945	0.0142

Tab. 6 Results of structural analysis of Co.

5.4.2 Discussion

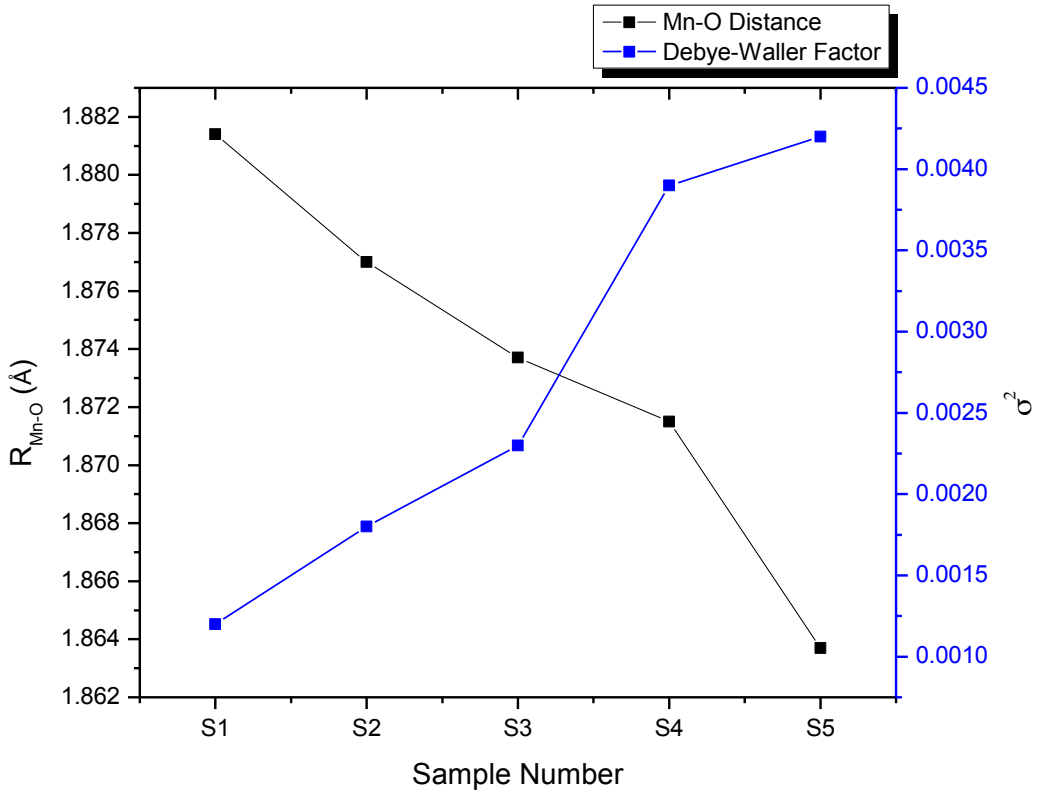

Fig. 31 First shell Mn-O bond length and Debye-Waller factor change during first charge.

The EXAFS signals of Mn, Ni and Co ions in $Li[Li_{0.2}Mn_{0.56}Ni_{0.16}Co_{0.08}]O_2$ was fitted by Gnxas. Bond length data and the corresponding Debye-Waller factor were extracted from the Fitheo output file and plotted in Fig. 31, Fig. 32, Fig. 33.

For Mn first shell, a coordination number of 6 was used to calculated Mn-O bond distance. As shown in Fig. 31, the first shell bond distance displays only minor change of around 0.02Å and gradually shortens during the course of initial charge. This could be considered constant compared with that of Ni and Co. At the same time, a progressive increase of Debye-Waller factor can be observed which indicates an increment of structural disorder. This phenomenon is in good agreement with conclusion obtained from the pre-edge analysis where a gradual increase of

intensities for both peak 1 and peak 2 could be observed.

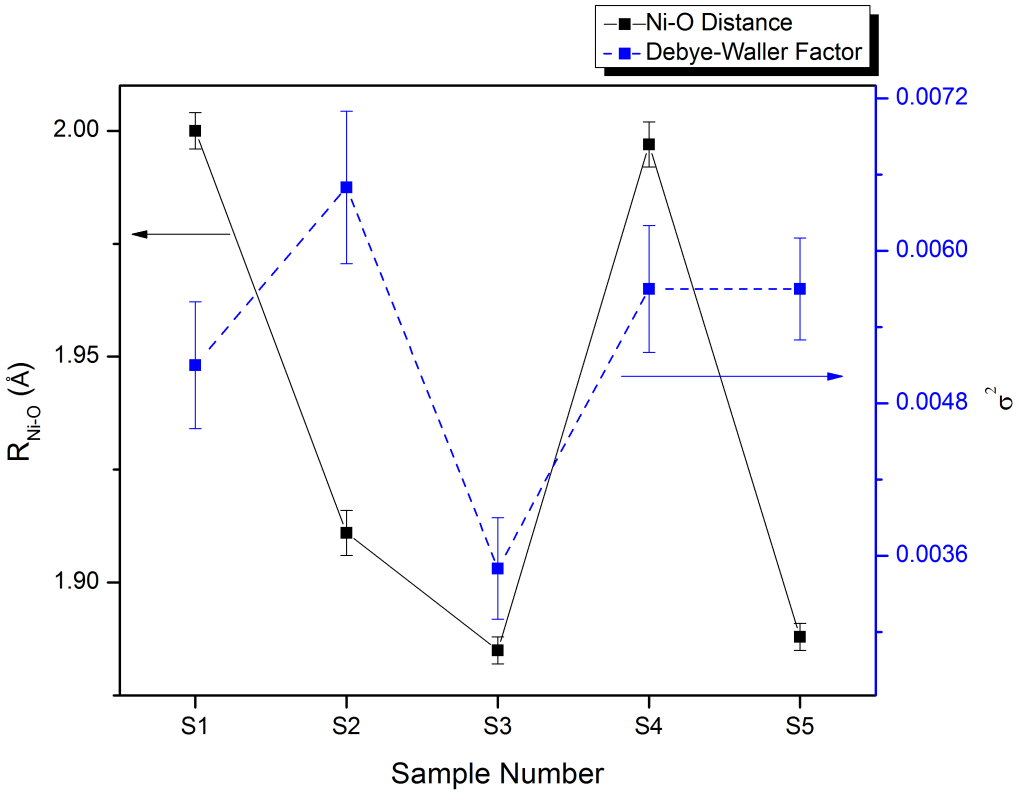

Fig. 32 First shell Ni-O bond length and Debye-Waller factor change during first charge. Error bars reflect the uncertainties in measuring the exact values.

For Ni first shell, a coordination number of 6 was used to calculate Ni-O bond distance although some errors might be introduced in the case of Ni^{3+} (Jahn-Teller active ion).[39] As shown in Fig. 32, the first shell bond distance displays a variation of more than 0.1Å during charging from point 1 to point 3, which is a relatively large structural modification compared with Mn. The same process is reckoned to be accompanied by Ni oxidation from +2 to +4 as the Li content increase. The Ni-O bond distance at point 3 and 5 of around 1.89Å agrees with previously reported Ni^{4+}-O distance observed in complexes such as $KNiIO_6$ (~1.88 Å).[40] This confirms the complete oxidation of Ni^{2+} to Ni^{4+}.

Second shell distances were also probed which showed a slight variation of less than 0.03Å. It is worth mentioning that other metals like Co or Mn might well be present in the second shell due to metal migration during Li extraction/insertion, but the amplitude of which can not be differentiated by XAS because of the close Z value in

the periodic table. Consequently they are considered Ni and coordination number were fixed at 6 for both the first and the second shell.

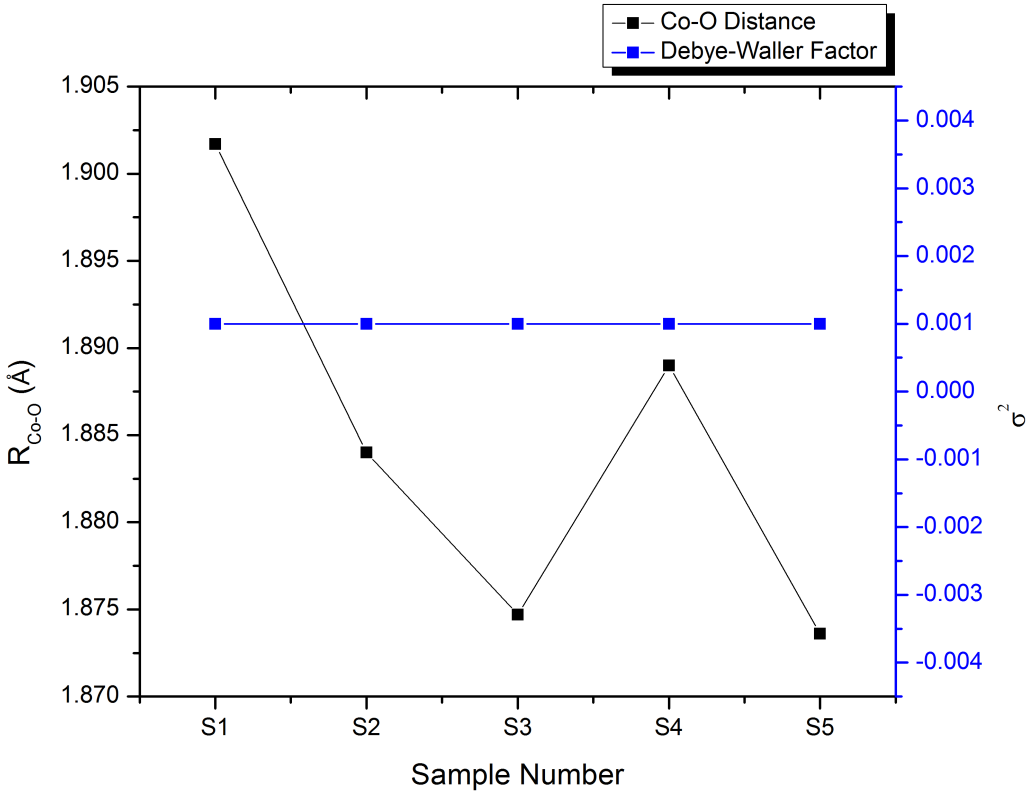

Fig. 33 First shell Co-O bond length and Debye-Waller factor change during first charge.

First shell distances for Co behave in a similar manner as Ni with a less variation of around 0.03Å, which is only 1/3 of that for Ni-O. This might indicate a smaller change of Co valent state compared with Ni, as demonstrated also from pre-edge analysis. Research works on similar LLOs normally report on Co^{3+} in the pristine sample that is oxidized to Co^{4+} during electrochemically charging. [13] The smaller variations of Co first shell distance compared with Ni can also be explained by crystal field theory and relative ionic radii. Since d orbitals in an octahedral crystal field splits into triply-degenerate t_{2g} and doubly-degenerate e_g with higher energy, the electronic configuration of redox species Co^{3+}/Co^{4+} can be represented as $t_{2g}^6 e_g^0$ / $t_{2g}^5 e_g^0$, whereas for $Ni^{2+}(Ni^{3+})/Ni^{4+}$ it can be represented as $t_{2g}^6 e_g^2$ $(t_{2g}^6 e_g^1)$/ $t_{2g}^6 e_g^0$. During initial charging, only the t_{2g} degenerate set undergoes modifications for Co which lead up to minor change in the ionic radius (R_{Co}^{3+}~0.54Å/ R_{Co}^{4+}~0.53Å). At the same time, the change takes place between lower

t_{2g} and higer e_g degenerate set, which would induce a larger variation in ionic radius (R_{Ni}^{2+}~0.69Å/ R_{Ni}^{3+}~0.56Å/ R_{Ni}^{4+}~0.48Å).

In the present project no relevant changes of the Debye-Waller factor for Co first shell is reported. Further investigation of parameter setting for program Fitheo input is still needed to obtain a more precise outcome.

6. Concluding Remarks

6.1 Reversibility

Fig. 34 and Fig. 35 shows variations of normalized pre-edge peak positions for Co and Ni K-edge during charge-discharge:

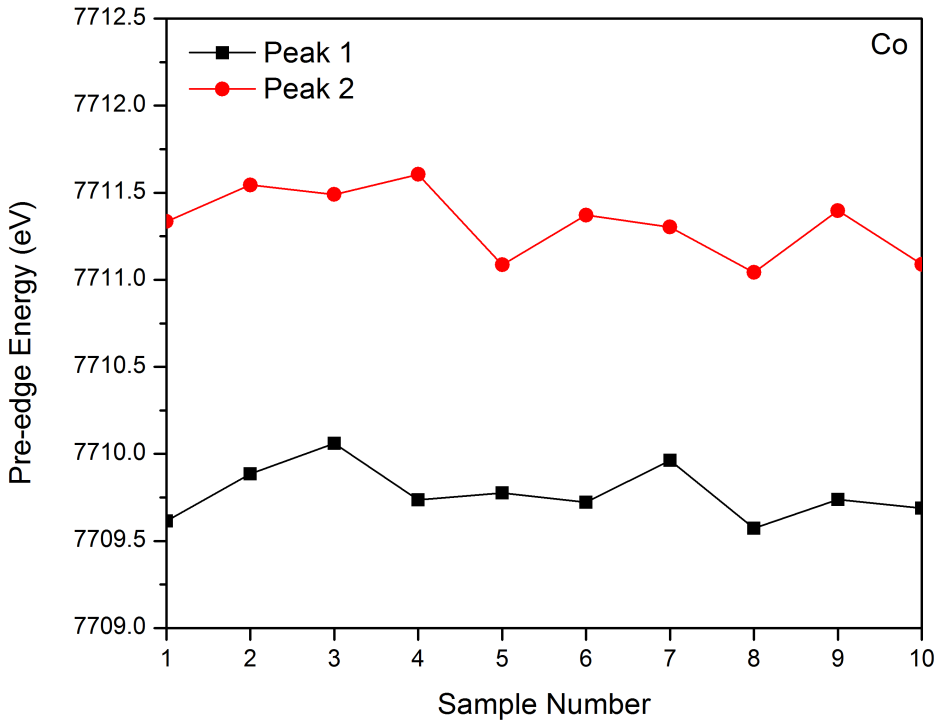

Fig. 34 Variations of normalized pre-edge peak positions for Co K-edge during charge-discharge.

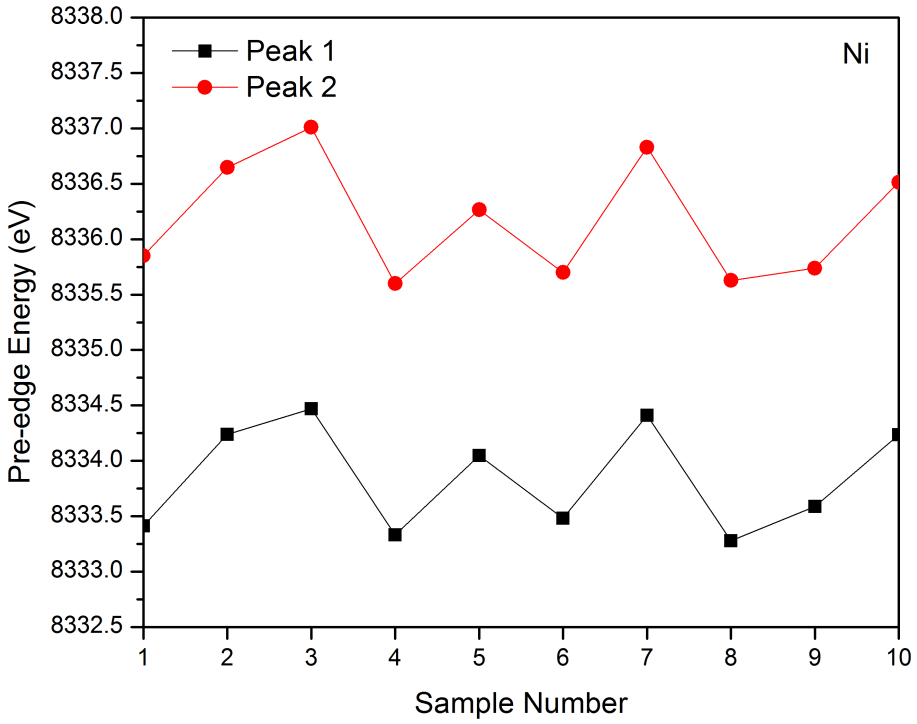

Fig. 35 Variations of normalized pre-edge peak positions for Ni K-edge during charge-discharge.

As can be seen, in the charge process to point 5 and subsequent discharge to point 8, the positions of the two pre-edge peaks for Co exhibit mirror-like variation with point 5 being the central symmetry. It can also be observed in the first discharge and second charge process from point 5 to point 10, which indicate good circling reversibility for the current Li-rich battery material in terms of electronic configuration. The change of Ni pre-edge energy exhibits the same trend with bigger variations between each measurement, reflecting the relative bigger range of change in oxidation states.

The same phenomenon can be seen in the first shell metal-oxygen distance as well as second shell metal-metal distance for Ni and Co respectively (Fig. 36 and Fig. 37). A mirror-like variation of bond distances is evident which confirms rather good reversibility from structural point of view. The distance profile of Co appears in accordance with Ni with exceptional lengthening at point 4 and 6, the hypothetical reason of which has been accounted for in previous sections. Note that this slight increase in bond length at the end of charge is generally observed in similar cathode

materials [30] but especially apparent for Li-rich samples. This phenomenon might be correlated with the higher capacity found for Li-excess layered transition-metal oxides.

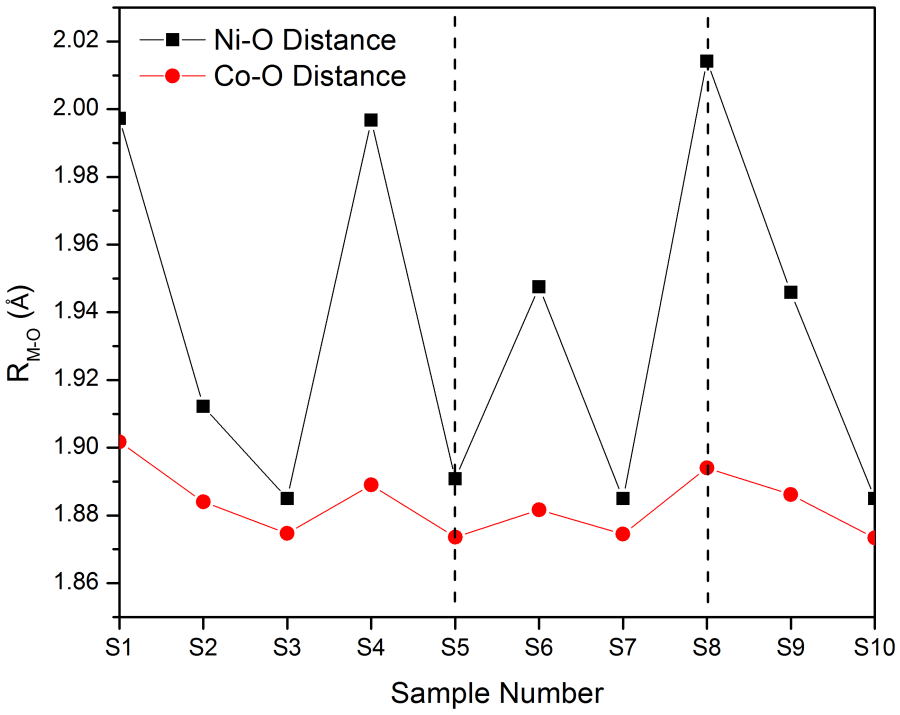

Fig. 36 First shell metal-oxygen bond length changes during charge-discharge for Ni and Co.

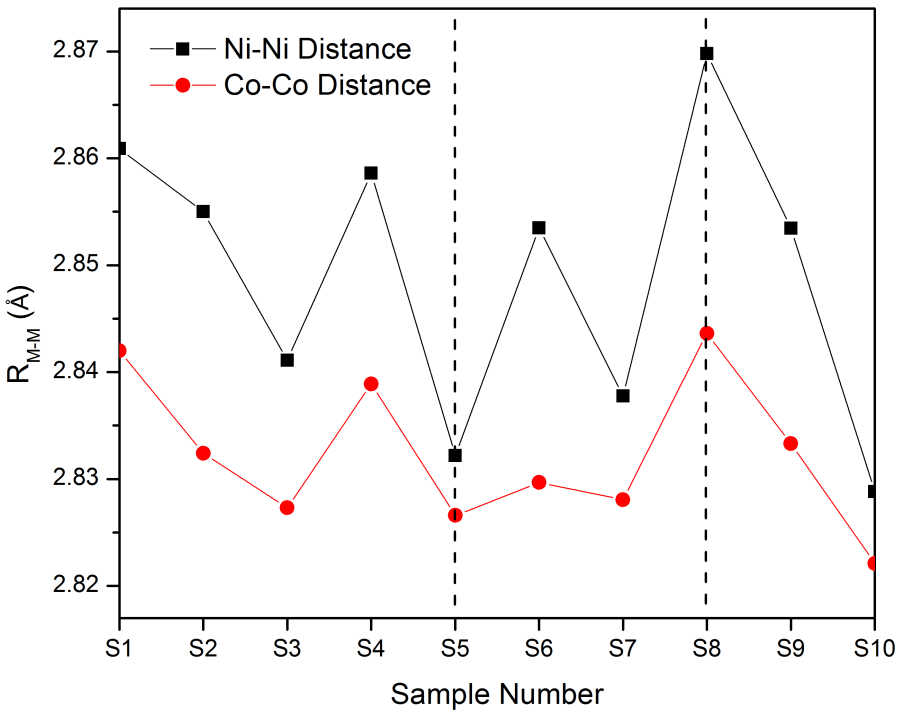

Fig. 37 Second shell metal-metal bond length changes during charge-discharge for Ni and Co.

Comparison of XANES spectra of the starting points of initial charge as well as of second charge (sample 1 and 8) exhibits a good match of peak profile (Fig. 38, Fig. 39, and Fig. 40). Slight difference of intensities for all three elements are observed which might possibly due to structural modification as well as atomic vacancies generated during initial charge. A more logical comparison could be made between the starting point of the second charge and third charge, which possess the same voltage, for reversibility examination, if experiment allows. The ending points of initial charge and second charge (sample 5 and 10) overlap completely, which indicates favorable structural stability as well as cycling performance.

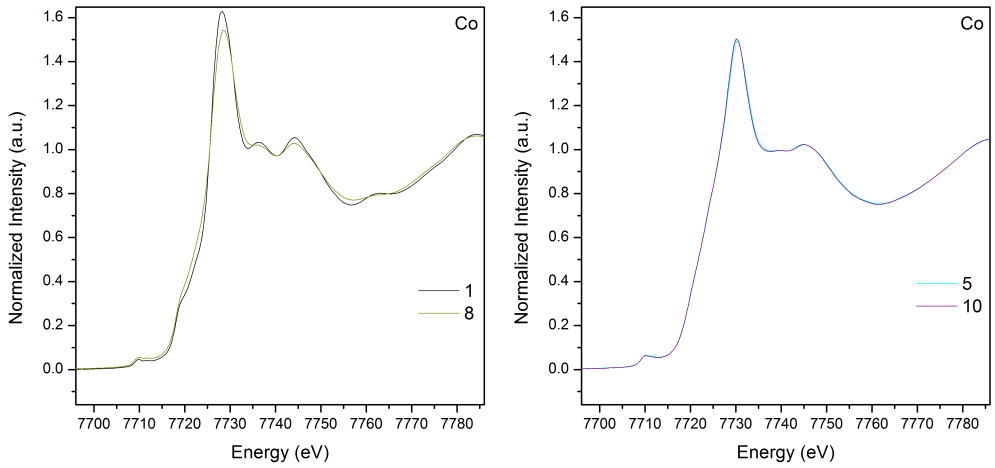

Fig. 38 Normalized Co K-edge EXAFS spectra of the comparison two starting points/ending points of the charge processes.

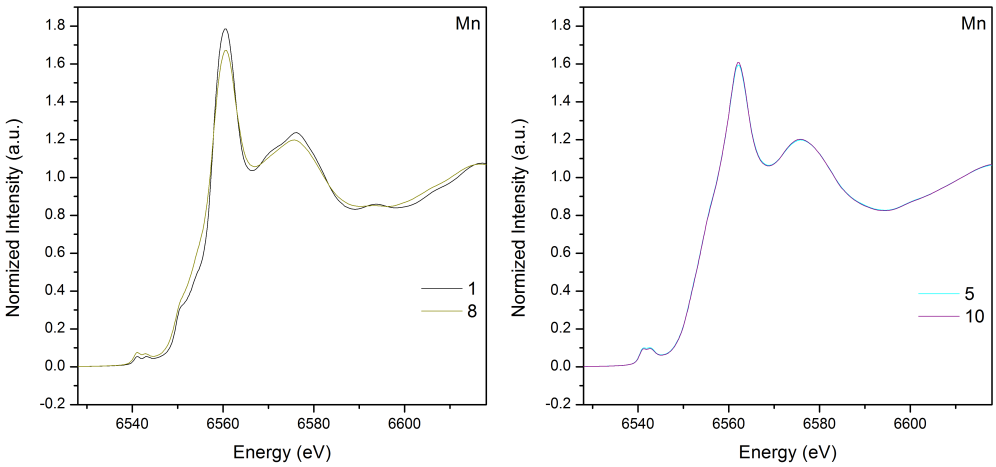

Fig. 39 Normalized Mn K-edge EXAFS spectra of the comparison two starting points/ending points of the charge processes.

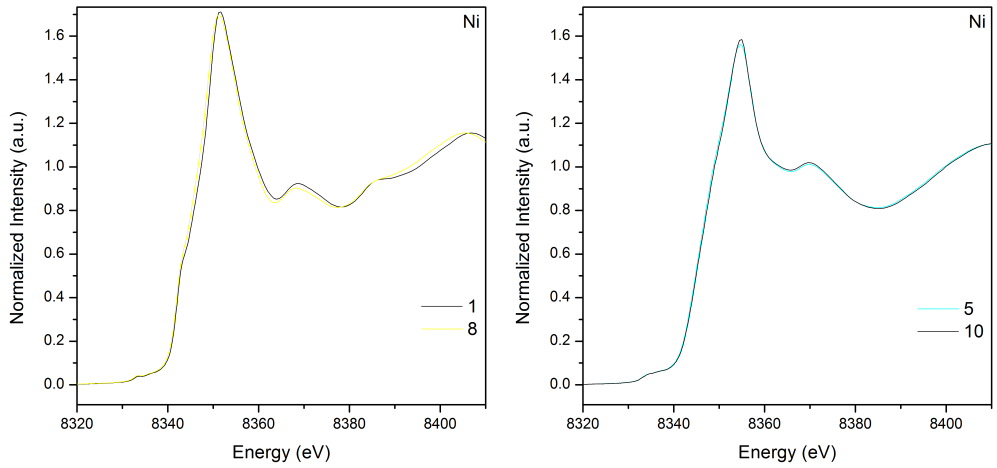

Fig. 40 Normalized Ni K-edge EXAFS spectra of the comparison two starting points/ending points of the charge processes.

6.2 Compatibility of Sample 1 and 4

It is also evident from Fig. 32 that sample 3 gives the smallest value for Ni-O bond distance as well as Debye-Waller factor while the behavior of sample 4 appears similar to sample 1. Comparison of parameters of Ni sample 1 and sample 4 can be seen in Tab. 7.

	Sample 1	**Sample 4**	**Δ (S1-S4)**
Pre-edge 1 (eV)	8333.4	8335.9	2.5
Pre-edge 2 (eV)	8333.3	8335.6	2.3
Edge position (eV)	8349.4	8348.8	-0.6
First shell distance (Å)	1.9973	1.9968	0.0005
First shell DW Factor	0.0051	0.0057	0.0006

Tab. 7 Comparison of parameters of Ni sample 1 and sample 4.

An oxygen reduction process on the electrode surface has been reported by Yabuuchi *et al.* [13] in account for this behavior. Oxygen release on the voltage plateau during initial charge results in the reduction of Ni ion from a +3/+4 mix state to +3/+2 mix state and the further charge to 4.8V will re-oxidate Ni ion to a higher valent state. This has been previously observed in gas evolution by in situ

differential electrochemical mass spectroscopy (DEMS).[39] But a smaller weight change than theoretical calculation during initial charge leads to another mechanism, which involves decomposition of electrolyte while transitional metals are reduced simultaneously.[23] This resemblance of sample 1 and 4 is first discovered in the present project which might be attributed to the *ex situ* approach of measurement that allows enough time for battery material to reach equilibrium.

6.3 Charge Compensation Mechanism

The reversibility capacity of $Li[Li_{0.2}Mn_{0.56}Ni_{0.16}Co_{0.08}]O_2$ during first charge was evaluated according to valence changes of Mn, Ni and Co to a limit of tetravalent state. Charging ends when all metals are oxidized to a tetravalent state. The amount of Li extraction was not utilized as a calculation parameter as Li could not be completely extracted from the material. We assumed a two-electron reaction for Ni and one-electron reaction for Co. Valent state for Mn remains constant according to pre-edge analysis so it is not included in the capacity calculation. The reversibility capacity of this cathode material is estimated to be 126mAh/g, which is actually in accord with the practical capacity at point 3 (105mAh/g). The slightly lower experimental capacity is anticipated due to incomplete oxidation of Ni and Co.

As for extra capacity from point 3 to 4, we believe in a partial oxidation of O^{2-} in our layered compound, which gives rise to Ni reduction from +4 oxidation state back to +2,[24] accompanied by possible Ni migration to Li layer, filling Li vacancies as lithium extraction.

Further charging from point 4 (~4.7V) to point 5 (4.8V) generates an experimental capacity of 117mAh/g. The theoretical value was also calculated assuming two-electrons loss for Ni and 0.5 for Co. The electron loss was determined according to Co first shell bond distance change from EXAFS analysis, which, to some extent, reflects variation of oxidation state. As can be seen in Fig. 33, Co-O bond length modification from sample 4 to 5 is about half of that from sample 1 to 3. Theoretical capacity was approximated to be 113mAh/g which agrees quite well with observed value. This could indicate a simple oxidation process of transitional metals during charging from point 4 to 5 without complex reactions concerning oxygen gas or electrolyte.

6.4 Structural Modification

The doping metals Ni and Co play a key role in maintaining the layered structure during cycling by keeping Mn in the tetravalent state based on many spectroscopic

investigations and theoretical calculations. [41,32] Layered $LiMnO_2$ was found to undergo a phase transformation to a spinel structure when half lithium is extracted, which negatively affect reversible capacity to a large extent. On the other hand, by replacing a part of nickel with cobalt and manganese, nickel is kept in the nickel layer instead of lithium layer, which assists in ordering the structure and increasing the lithium diffusion coefficient. [4] The Li-rich composition could accommodate certain amount of lithium in the transition metal layer without considerable disturbance of the $R\bar{3}m$ structure of the material. [42] But a certain degree of structural rearrangement could still be observed during initial charge.

The XANES spectra of sample 1-3 have evidenced a strong shift to higher energy at Ni K-edge and a smaller one of the Co K-edge all of which indicate an oxidation process. Here all the metals are already of the +4 oxidation state in the middle of the charge process (point 3). The extra capacity in the following charge can be explained by considering, as suggested by Yabuchi *et al*., [13] Oxygen evolution from 6c site upon the first charge with simultaneous removal of lithium from the 3a site that causes some in-plane caution rearrangements. As the structural rearrangements can promote metal migration to the 3a site previously occupied by the lithium, we could reckon that there exists a partial Ni migration also from 3b sites to 3a sites during reduction from point 3 to 4, which results in a significant decrease in the average Ni-O bond length. This is not surprising as the ionic radius of Ni^{2+} 6-coordinated octahedral environment (0.69Å) is similar to those of Li^{+} (0.76 Å). Metal-oxygen distance at 3a site (~2.11 Å) and 3b site (~1.95) proves in agreement with experimental value. Distances were taken at the average of the corresponding value of LiNiO2 [43] (Ni-O: 1.97 Å, Li-O: 2.12 Å) and LiCoO2 [37] (Ni-O: 1.92 Å, Li-O: 2.09 Å) respectively. At present it is impossible to tell which is the number of Ni atoms that undergo migration. Measurements of XRD of similar samples indicate this number to be 10-20%, [24] but we believe this number can be even higher in our cathode material, as the XAS probe the bulk of the material. Similar behavior is seen for the Co, with a less extent, whereas the Mn site undergoes structural rearrangements of the octahedral mainly. As also evidenced by the pre-edge analysis.

APPENDIX

GNXAS Package

Three major packages have been developed in an attempt to correctly account for multiple scattering contributions based on theoretical calculations. They are developed by different groups and differ mainly in the way multiple scattering (MS) is introduced and in the treatment of configurational average effects.

GNXAS, software of choice in the present project, was developed by the Filipponi Dicicco research group in Italy based on MS calculations and a rigorous fitting procedure of the raw experimental data. [44] Particular features include 6 separate programs that allow access to every stage of the calculation and successful treatment in case of liquid phase or disordered systems. The EXCURVE package was developed by Daresbury *et al*. which was actually the first user-oriented package to be developed. It simulates EXAFS spectra using rapid curved wave theory from the parameters of the radial shells of atoms surrounding the central atom. An extensive application of polarized MS to the analysis of surface EXAFS has been successfully performed. The FEFF package was developed by the Seattle group, that is mainly based on the fast separable approximation by Rehr and Albers.

The GNXAS software development project was initiated the year 1990 in order to facilitate the scientists in experiment preparation as well as subsequent data analysis. The name GNXAS originates from the n-atom distribution functions g_n, the features of which are compared with the experimental XAS signal. The software has been widely tested and applied to a variety of systems including simple gas-phase molecules, clusters, nanocrystals, molecular solids and liquids, crystalline and liquid metals, solid and molten salts, amorphous solids and glasses, solutions, high-T_c superconductors, and biological matter. Its success is mainly due to the possibility of calculating the actual $\gamma^{(n)}$ signals associated with n-body configurations, that account for an infinite number of MS paths, and to the correct treatment of the configurational average of MS signals that allows us to fit correlated vibrational motion in three-body configurations. [44]

The GNXAS package includes five major EXAFS data-analysis programs, which constitute the main part of the package and are among the most advanced codes available. Several other utility programs for sample optimization, automatic background subtraction, and edge analysis are also provided but will not be covered in the present project.

The backbone of the GNXAS package is composed of three main codes, in logical sequence:

1) Phagen: potential and phase shift generation.
2) Gnxas: signal calculation for reference geometries.
3) Fitheo: advanced fitting of the experimental data.

Two other programs are able to prepare automatically the input for Phagen and Gnxas starting directly from model molecular positions or crystallographic data. These are particularly useful in the case of complex structures where the configuration counting is not trivial.

4) Crymol: allows one to treat complex molecular and crystallographic structures providing input information for Phagen, Gnpeak, and Xanes; the program identifies prototypical phase-shift atoms and select a suitable cluster of atoms for successive XAS calculations.
5) Gnpeak: based on a general algorithm able to identify inequivalent two-body, three-body and four-body configurations in various structures providing valuable input information for Gnxas.

A simplified logical flow-chart related to these data analysis programs is illustrated in the figure below:

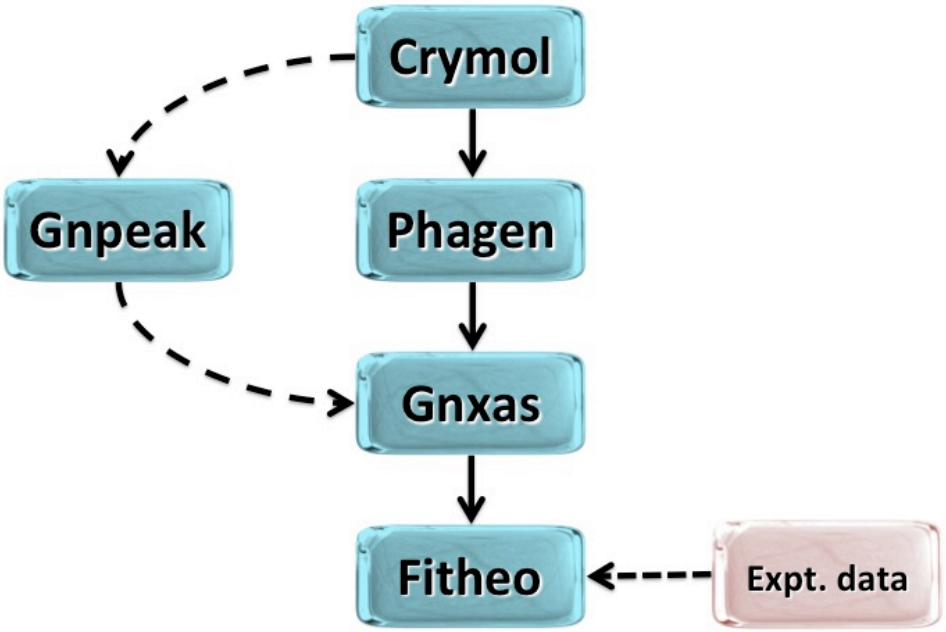

Fig. 41 Main scheme of the GNXAS package.

Bibliography

1 J.-M. Tarascon, M. Armand. *Nature*, 414 (2001), 359-360.

2 Y. W. Tsai, B. J. Hwang, G. Ceder, H. S. Sheu, D. G. Liu, and Lee, J. F. *Chem. Mater.*, 17 (2005), 3191-3199.

3 H. Xia, L. Lu, Y. S. Meng, G. Ceder. *J. Electrochem. Soc.*, 154, 4 (2007), A337-A342.

4 M. S. Whittingham. *Chem. Rev.*, 104 (2004), 4271-4301.

5 B. Xu, D. Qian, Z. Wang, Y. Meng. *Mater. Sci. Eng. R-Rep.*, 73 (2012), 51-65.

6 P. Verma, P. Maire, P. Novak. *Electrochimica Acta*, 55 (2010), 6332-6341.

7 H. Yu, H. Zhou. *J. Phys. Chem. Lett.*, 4 (2013), 1268-1280.

8 T. Ohzuku, U. Makimura. *Chem. Lett.* (2001), 744-745.

9 M. S. Whittingham. *Science*, 192 (1976), 1126-1127.

10 N. Yabuuchi, T. Ohzuku. *Journal of Power Sources*, 146 (2005), 636-639.

11 M. M. Thackeray, C. S. Johnson, J. T. Vaughey, S. A. Hackney. *J. Mater. Chem*, 15 (2005), 2257-2267.

12 Z. H. lu, D. D. Macneil, J. R. Yang, M. Balasubramanian, J. Mcbreen, C. P. Grey. *Electrochem. Solid-State Lett.*, 4 (2001), A191-A194.

13 N. Yabuuchi, K. Yoshii, S.-T. Myung, I. Nakai, S. Komaba. *J. Am. Chem. Soc.* , 133 (2011), 4404-4419.

14 C. R. Fell, K. J. Carroll, M. F. Chi, Y. S. Meng. *J. Electrochem. Soc.* , 157 (2010), A1202-A1211.

15 H. J. Yu, H. J. Kim, Y. R. Wang, P. He, D. Asakura, Y. Nakamura, H. S. Zhou. *Phys. Chem. Chem. Phys.*, 14 (2012), 6584-6595.

16 J. Bareno, C. H. Lei, J. G. Wen, S. H. Kang, L. Petrov, D. P. Abraham. *Adv. Mater* (2010), 1122-1127.

17 A. Boulineau, L. Simonin, J. F. Colin, E. Canevet, L. Daniel, S, Patoux. *Chem. Mater.*, 24 (2012), 3558-3566.

18 W. S. Yoon, N. Kim, X. Q. Yang, J. Mcbreen, C. P. Grey. *J. Power Sources* , 119 (2003), 649-653.

19 T. Ohzuku, M. Nagayama, K. Tsuji, K. Ariyoshi. *J. Mater. Chem*, 21 (2011), 10179-10188.

20 B. Ammundsen, J. Paulsen, L. Davidson, R. S. Liu, C. H. Shen, J. M. Chen, L. Y. Jang, J. F. Lee. *J. Electrochem. Soc.*, 149 (2002), A431-A436.

21 K. A. Jarvis, Z. Q. Deng, L. D. Allard, A. Manthiram, P. J. Ferreira. *Chem. Mater*, 23 (2011), 3614-3621.

22 Z. H. Lu, J. R. Dahn. *J. Electrochem. Soc.* , 149 (2002), A815-A822.

23 M. Jiang, B. Key, Y. S. Meng, C. P. Grey. *Chem. Mater*, 21 (2009), 2733-2745.

24 A. R. Armstrong, M. Holzapfel, P. Novak, C. S. Johnson, S. H. Kang, M. M. Thackeray, P. G. Bruce. *J. Am. Chem. Soc*, 128 (2006), 8694-8698.

25 N. Tran, L. Croguennec, M Menetrier, F. Weill, P. Biensan, C. Jordy, C. Delmas. *Chem. Mater*, 20 (2008), 4815-4825.

26 B. Xu, C. R. Fell, M. F. Chi, Y. S. Meng. *Energy Environ. Sci.* , 4 (2011), 2223-2233.

27 C. P. Grey, W. S. Yoon, J. Reed, G. Ceder. *Electrochem Solid-State Lett.* , 7 (2004), A290-A293.

28 M. Giorgetti. *ISRM Mater. Sci.*, 2013 (2013), 1-22.

29 Y. Gao, M. V. Yakovleva, W. B. Ebner. *Electrochem. Solid-State Lett.*, 1 (1998), 117-119.

30 A. Deb, U. Bergmann, S. P. Cramer, E. J. Cairns. *J. Appl. Phys*, 97 (2005), 113523.

31 D. Y. W. Yu, K. Yanagida, Y. Kato, H. Nakamura. *Electrochem. Commun.*, 156 (2009), A417-A429.

32 S. -H. Kang, S. H. Park, C. S. Johnson, K. Amine. *J. Electrochem. Soc.*, 154 (2007), A268-A274.

33 T. Yananoto. *X-Ray Spectrom.*, 37 (2008), 572-584.

34 R. A. Bair, W. A. Goddard. *Phys. Rev*, 22 (1980), 2767-2776.

35 E. Cannillo, F. Mazzi, G. Rossi. *Acta Crystallogr.* , 21 (1966), 200-208.

36 M. Pouchard, A. Villesuzanne, J. -P, Doumerec. *Solid State Chem.*, 162 (2001), 282-292.

37 J. Zhu, T. Vo, D. Li, R. Lu, N. M. Kinsinger, L. Xiong, Y. Yan, D. Kisailus. *Cryst. Growth Des.*, 12 (2012), 1118-1123.

38 A. Filipponi, A. Cicco. *Task Quarterly*, 4 (2000), 575-669.

39 A. Ito, Y. Sato, T. Sanada, M. Hatano, H. Horie, Y. Ohsawa. *J. Power Sources*, 196 (2011), 6828-6834.

40 W. E. O'Grady, K. I. Pandya, K. E. Swider, D. A. Corrigan. *J. Electrochem. Soc.* , 143 (1996), 1613-1617.

41 S. H. Kang, J. Kim, D. Abraham, M. E. Stoll, Y.-K. Sun, K. Amine. *J. Power Sources*, 112 (2002), 41-48.

42 S. H. Choi, O. A. Shlyakhtin, J. Kim, Y. S. Yoon. *J. Power Sources* , 140 (2005), 355-360.

43 P. Kalyani, N. Kalaiselvi. *Sci. Technol. Adv. Mater* , 6 (2005), 689-703.

44 A. Filipponi. *Phys. Rev.*, 52 (1995), 122-134.

45 J. Breger, M. Jiang, N. Dupre, Y. S. Meng, Y. Shao-Horn, G. ceder, C. P. Grey. *J. Solid State Chem*., 178 (2005), 2575-2585.

46 W. E. Jackson, F. Farges, M. Yeager, P. A. Mabrouk, S. Rossano, G. A. Waychunas, E. I. Solomon, G. R. Brown. *Ceochim. Cosmochim. Acta*, 69 (2005), 4315-4332.